Petroleum Research 11 (2026) 1–16

Contents lists available at ScienceDirect

Petroleum Research

journal homepage: http://www.keaipublishing.com/en/journals/petroleum-research/

Full Length Article

Diagenetic calcite-dolomite-pyrite in the organic-rich shales of the Early Silurian Longmaxi Formation in the Yangtze block, South China

Yuexiang Hao [a], Yi Liu [a], Yibo Zhou [a], Jiexin Li [a], Yumeng Jiang [a], Chao Qian [a], Xiangrong Yang [b,c,*]

[a] CNPC Chuanqing Drilling Engineering Company Ltd, Chengdu 610051, China
[b] College of Geosciences, Yangtze University, Wuhan 430100, China
[c] Laboratory of Reservoir Microstructure Evolution and Digital Characterization, Wuhan 430100, China

ARTICLE INFO

Article history:
Received 29 April 2025
Received in revised form
29 July 2025
Accepted 30 July 2025
Available online 6 August 2025

Keywords:
Black shale
Carbon isotope
Sulfur isotope
Calcite
Dolomite
Pyrite

ABSTRACT

Carbonate minerals (calcite and dolomite) and pyrite are important brittle minerals in organic-rich shales; however, the mechanism of their formation is still uncertain. This study examined the formation of pyrite and carbonate minerals (mainly calcite and dolomite) in the shales of Longmaxi (LMX) Formation through a combination of petrological and geochemical techniques. The results demonstrated that two types of carbonate minerals (calcite and dolomite) and multiple-types of pyrite were identified in the studied shales. The carbonate minerals comprise (1) subhedral to euhedral calcite and dolomite with large diameters (>10 μm), along with low Fe (<2%) and Mn (<0.2%) contents, and (2) calcite and dolomite cement, along with high Fe (>2%) and Mn (>0.2%) contents. The pyrite is primarily composed of framboidal pyrite, infilled framboidal pyrite, pyritic masses, and euhedral pyrite. This study suggests that depositional and diagenetic processes had significant influences on the formation of calcite-dolomite-pyrite in organic-rich shales. In the synsedimentary stage, the expansion of anoxic seawater contributed to the enrichment of organic matter in the shales of lower LMX Formation. In the early diagenesis stage, both the microbial sulfate reduction (MSR) and sulfate-driven anaerobic oxidation of methane (SD-AOM) would generate abundant CO_2, which together with the consumption of SO_4^{2-} further contribute to the precipitation of carbonate minerals (calcite and dolomite). In addition, the MSR would also release ^{32}S-enriched H_2S and result in the formation of framboidal pyrite/infilled framboids/pyritic masses with low $\delta^{34}S$ values (<0‰). However, the SD-AOM would result in the precipitation of euhedral pyrite with high $\delta^{34}S$ values (>20‰) and high Co contents (>700 μg/g). In the late diagenesis stage, carbonate cements with high Fe and Mn contents formed due to the diagenetic fluids (high HCO_3^- Mg^{2+}, Fe^{2+}, Mn^{2+} concentrations). Overall, the sulfate-driven anaerobic oxidation of methane (AOM) during early diagenesis in sediments constitutes a key process influencing methane release, in which case extensive methane release during this period may have contributed to Early Silurian global warming.

© 2025 Chinese Petroleum Society. Publishing services by Elsevier B.V. on behalf of KeAi Communications Co. Ltd. This is an open access article under the CC BY-NC-ND license (http://creativecommons.org/licenses/by-nc-nd/4.0/).

1. Introduction

The black shales of the early Silurian Longmaxi (LMX) Formation in the Upper Yangtze region are regarded as important marine stratigraphic assemblages (Yan et al., 2015; Yang et al., 2020; Zou et al., 2010). Their significance stems from being a vital target stratum for gas-bearing shales in the Sichuan Basin, South China (Zou et al., 2010). Previous studies have suggested that intense volcanic activity (Li et al., 2021) leads to high primary productivity (Lu et al., 2019; Yan et al., 2015) and anoxia of bottom seawater. Moreover, enhanced continental weathering, tectonism and upwelling were also found to be the dominant factors driving the deposition of organic-rich shales in the LMX Formation (Ge et al., 2019; Liu et al., 2017; Yang et al., 2021, 2023, 2024).

The black shales of the LMX Formation are primarily

* Corresponding author. College of Geosciences, Yangtze University, Wuhan 430100, China.
E-mail address: m15727044911@163.com (X. Yang).
Peer review under the responsibility of Editorial Office of Petroleum Research.

https://doi.org/10.1016/j.ptlrs.2025.07.009
2096-2495/© 2025 Chinese Petroleum Society. Publishing services by Elsevier B.V. on behalf of KeAi Communications Co. Ltd. This is an open access article under the CC BY-NC-ND license (http://creativecommons.org/licenses/by-nc-nd/4.0/).

characterized by high contents of quartz, clay minerals, and carbonate minerals (calcite and dolomite), along with minor amounts of feldspar, pyrite, and barite (Yan et al., 2021; Yang et al., 2018; Zan et al., 2022). Quartz, pyrite, and carbonate minerals are important brittle minerals that are extensively present in the organic-rich shales of the LMX Formation (Gao et al., 2019; Yang et al., 2018; Zhao et al., 2017). The quartz in the shales was derived from terrigenous detritus, siliceous organisms, and illitization (Yang et al., 2018; Zhao et al., 2017), moreover, these authigenic quartz acts as a cement that fills pore spaces and hence occupies a certain proportion of the shale porosity (Fishman et al., 2012).

Recently, an increasing number of studies have revealed that carbonate minerals (calcite and dolomite) and pyrite are significant brittle minerals that developed in the organic-rich shales of the LMX Formation (Gao et al., 2019; Chen et al., 2023a, 2023b), and they are conducive to the formation of fractures induced by artificial fracturing during the subsequent stages of development (Liu et al., 2019; Xie et al., 2020). Generally, carbonate minerals and pyrite provide the rigid framework and they can preserve primary pores, which provide a high storage capacity for the organic matter and shale gas (Chen et al., 2023b). The formation of carbonate minerals and pyrite in shales could be influenced by the cementation, recrystallization, dissolution during the depositional and diagenetic processes (Chen et al., 2017, 2020; Li et al., 2020; Wu et al., 2020). As a result, the various occurrences of carbonate minerals and pyrite can cause changes in the micro-scale pore structure and mechanical properties of the shale (Chen et al., 2023; Li et al., 2024). For example, the content of carbonate minerals is positively correlated with the abundance of micropores (<2 nm) in the Alberta Belle Fourche and Second White Specks formations, while the dissolution of carbonate minerals in the Haynesville Shale can form a pore network with a good connectivity that is closely related to the occurrence of macropores (>50 nm) (Chalmers et al., 2012; Furmann et al., 2016; Hu et al., 2015). Overall, the diagenetic evolution of these minerals has a significant influence on hydrocarbon generation, storage, and reservoir formation in shales (Chen et al., 2023b; Li et al., 2024).

The formation mechanisms of pyrite and carbonate minerals are governed by depositional and diagenetic processes (Cai et al., 2003, 2021, 2022, 2023; Chen et al., 2017; Slack et al., 2021; Zan et al., 2020, 2022; Liang et al., 2024a, b). Notably, the precipitation of carbonate minerals and pyrite is associated with the evolution of organic matter, which is primarily regulated by shallow biological burial, as well as thermal deep burial processes in shales (Irwin et al., 1977; Liang et al., 2024a; b). The formation of pyrite in organic-rich shales is associated with the anoxia of bottom seawater in the synsedimentary stage, anaerobic oxidation of organic matter in the early diagenetic stage, and thermochemical sulfate reduction during late diagenesis in the late diagenetic stage (Bonnetti et al., 2020; Cai et al., 2003; Hu et al., 2018; Zuo et al., 2021). The calcite in shales could form in several ways, such as the dissolution and reprecipitation of calcareous organisms during the synsedimentary stage (Bordiga et al., 2013; Liang et al., 2024), microbial sulfate reduction (MSR), and anaerobic oxidation of methane (AOM) by sulfate (sulfate driven oxidation of methane: SD-AOM), or by Mn- and Fe-oxides in the early diagenesis stage (Cai et al., 2021, 2022, 2023; Hu et al., 2018), as well as the thermal decarboxylation of organic matter and thermochemical sulfate reduction (TSR) during the late diagenesis stage (Cai et al., 2003; Sun et al., 2021; Xie et al., 2020). Moreover, the dissolution and reprecipitation of calcareous organisms serve as vital Ca^{2+} sources for calcite (Bordiga et al., 2013; Liang et al., 2024). However, the depositional position must be shallower than the carbonate compensation depth (CCD) to provide an alkaline aqueous environment for the precipitation of these calcites (Beauchamp and Grasby, 2012; Lisitzin, 1972). The precipitation of dolomite is also regarded as an intrinsic biochemical process, wherein processes such as MSR and SD-AOM play key roles in facilitating dolomite precipitation at low surface temperatures (Hinrichs et al., 1999; Roberts et al., 2004; Sanchez-Roman et al., 2009; Liu et al., 2021).

The pyrite and carbonate minerals are widespread during the deposition and burial of organic-rich shales (Gregory et al., 2015; Sun et al., 2021; Liang et al., 2024a, 2024b). Generally, their contents could significant influence the microfracture and pore structure in shales (Liu et al., 2023; Liang et al., 2024a, 2024b), as a result, it is critical to understand the timing and influencing factors that govern the dissolution and formation of these minerals (pyrite: Liang et al., 2024a; carbonate minerals: Liang et al., 2024b). In this study, the organic-rich black shales of the early Silurian LMX Formation in the Sichuan Basin were selected to evaluate the formation mechanisms of pyrite and carbonate minerals (calcite and pyrite).

2. Geological setting

The South China Block was situated close to the equator during the Late Ordovician and Early Silurian periods. It was comprised of the Cathaysia Platform in the southeast and the Yangtze Platform in the northwest (Fig. 1A, Chen et al., 2004; Zhang et al., 2013), with the water depth increasing from Cathaysia to Panthalassic Ocean (Fig. 1B). A significant tectonic event, the Kwangsian Orogeny, occurred between the Late Ordovician and Early Silurian period. This event led to a series of paleo-uplifts and depressions, which resulted in an extrusion collision between the Yangtze and Cathaysia blocks (Chen et al., 2012). Fine-grain sediments were deposited within the sags on the Yangtze Platform. The Kwangsian Orogeny event led to a gradual upliftment of both the Cathaysia and Yangtze blocks from the ocean basin, which resulted in the formation of a continent (Chen et al., 2012).

The Sichuan Basin is located in the western part of the Yangtze Platform, with the Late Ordovician-Early Silurian stratum being divided into the Wufeng (WF) Formation at the bottom and LMX Formation at the top (Fig. 1C, Chen et al., 2004, 2012; Mou et al., 2014). In the Early Silurian, the LMX Formation was deposited above the WF Formation, with the lower part comprising siliceous and carbonaceous organic-rich shales and the upper part of argillaceous organic-poor shales (Fig. 1C).

This study considered a total of three outcrops and one borehole across the shallow to deep-water shelf, including the BD-1 borehole, Heizugou (HZG), Tekelin (TKL), and Weimohani (WMHN) outcrops (Fig. 1A–C). All the boreholes and sections were deposited in the southwest Yangtze Platform, and they were deposited on a shallow shelf (Fig. 1A). It was observed that the WF and LMX formations are predominantly composed of organic-rich shales in these borehole and sections (Fig. 1C). The shales in BD-1 borehole and HZG section are primarily composed of siliceous shales, argillaceous shales and calcareous shales (Fig. 1C). The shales in WMHN and TKL sections (Fig. 1C) are mainly dominated by calcareous shales, marlstones and limestones (Fig. 1C).

3. Materials and methods

3.1. Materials

In this study, a variety of shales were selected, including 36 samples from the BD-1 borehole, 47 from the WMHN section, 29 from the HZG section, and 41 from the TKL section (Fig. 1C). The weathered surfaces were removed, and the shales were then roughly crushed and washed with deionized water, followed by drying and grinding to a 200-mesh size for further analysis and testing.

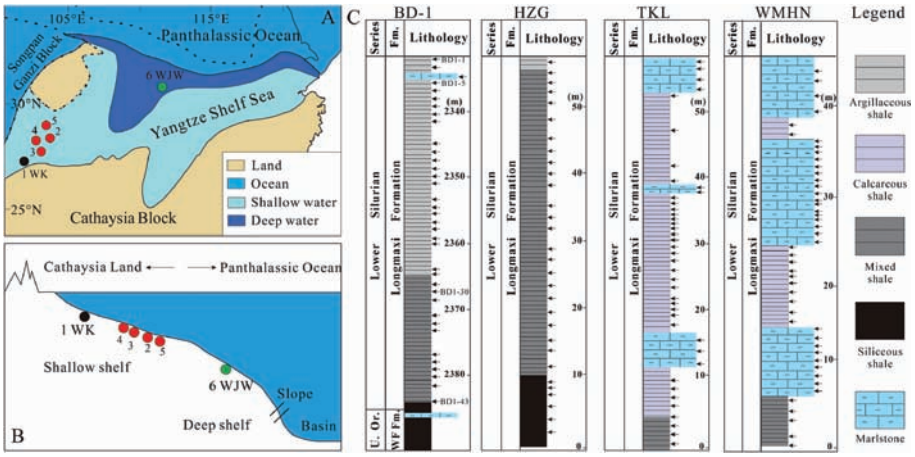


Fig. 1. (A) Paleogeographic map of the Yangtze Shelf Sea (modified from Chen et al., 2004; Zou et al., 2018), and the studied outcrops and borehole are presented; 1: Wuke (WK, Yang et al., 2021), 2: Weimohani (WMHN), 3: BD-1 borehole, 4: Heizugou (HZG), 5: Tekelin (TKL), 6:Wangjiwan (WJW, Yan et al., 2021); (B) Schematic cross section of the Late Ordovician Yangtze Shelf Sea showing estimated relative paleo-depths and study sections (modified from Zou et al., 2018). (C) The stratum across Ordovician - Silurian boundary in South China, including the Wufeng (WF) and Longmaxi (LMX) formations in ascending order.

3.2. Major and trace elements

The sample pretreatment of whole rock major element analysis was made by melting method. The flux is a mixture of lithium tetraborate, lithium metaborate and lithium fluoride (45:10:5), Ammonium nitrate and lithium bromide were used as oxidant and release agent respectively,The melting temperature was 1050 °C and the melting time was 15min. The major elements were measured by X-ray fluorescence spectrometry (XRF). The standard curve was prepared using the following national standard materials: standard rock sample GBW07101–14, standard soil sample GBW07401–08, and standard stream sediment sample GBW07302-12. The relative standard deviation (RSD) was less than 2%, and the analytical precision was greater than 5%.

Whole-rock trace element analysis was conducted using an Agilent 7700e ICP–MS, and the analytical precision was greater than 5%. The enrichment factors for U (U_{EF}) and Mo (Mo_{EF}) were calculated as $X_{EF} = [(X/Al)_{sample}/(X/Al)_{PAAS}]$, where PAAS represents the Post-Archean Australian Shale, X and Al represent the weight percent concentrations of the elements X and Al, respectively (Taylor and McLennan, 1985).

3.3. TOC

The total organic carbon (TOC) of the samples was determined using an Elementar Vario EL. Before the test, the samples were preleached in diluted hydrochloric acid (HCl) for 24 h. The analytical precision was greater than 2%.

3.4. Petrographic observation

The identification of petrofacies of shales are mainly based on the mineral contents in bulk rocks and minerals characteristics. The shales could be divided into siliceous (quartz-feldspar >50%), calcareous (carbonate minerals >50%), argillaceous (clay minerals >50%) and mixed (no minerals >50%) shales based on their mineral contents (e.g. quartz-feldspar, carbonate and clay mineral contents). Multiple-stage formation of minerals could be identified according to their morphological characteristics (e.g. euhedral, subhedral, cement).

3.4.1. X-ray diffraction (XRD)

The bulk samples were subjected to XRD analysis using a Rigaku automated powder diffractometer with CuKα radiation (40 kV, 40 mA). The diffracted beam was measured with a step size of 0.017°. Jade software was used to interpret the raw diffraction data and determine the mineral contents. The minerals (e.g., quartz, feldspar, clay) contained in the samples were identified by comparing the X-ray spectrum with a database (Joint Committee on Power Diffraction Standards-International Center for Diffraction Data (JCPDS-ICDD)).

3.4.2. SEM and electron probe

Scanning electron microscopy (SEM) images were taken at the China University of Geosciences using a field-emission scanning electron microscope (Quanta 450 FEG). SEM imaging was performed with secondary-electron (SE), back-scattered electron (BSE) and energy-dispersive spectroscopy (EDS) methods. The working distance between the probe and surface of the samples varied from 15.2 mm, and the spot size was 6 with the Vac.mode choosing HV (25 kV).

The quantitative analysis of the in situ major element contents of the minerals was completed by using an electron probe microanalyzer at Wuhan Sample Solution Analytical Technology Co., Ltd., Wuhan, China. The analysis was completed using a JEOL JXA-8230 instrument. The calibration standard samples for the content of major elements mainly included Ca, Mg, Fe, Sr, Mn in carbonate minerals and Fe, S, Co in pyrite.

3.5. In situ sulfur isotope analyses

In situ sulfur isotope analyses were performed using an MC–ICP–MS instrument (Neptune Plus) equipped with a Geolas HD excimer ArF laser ablation system, which was obtained from Wuhan Sample Solution Analytical Technology Co., Ltd. The laser instrument was set up for a background analysis of 30 s with a 5 mJ/cm^2 laser influence and a 2 Hz laser repetition rate. In-house references of pyrrhotite SP-Po-01 ($\delta^{34}S_{v\text{-}CDT} = 1.4 \pm 0.4‰$), chalcopyrite SP-CP-01 ($\delta^{34}S_{v\text{-}CDT} = 5.45 \pm 0.3‰$), and two synthetic Ag2S standards, IAEA-S-2 ($\delta^{34}S_{v\text{-}CDT} = 22.58 \pm 0.39‰$) and IAEA-S-3 ($\delta^{34}S_{v\text{-}CDT} = -32.18 \pm 0.45‰$), were analyzed repeatedly as unknown samples to verify the accuracy of the calibration method.

4. Results

4.1. Petrology

4.1.1. Lithofacies

All the shales in this study are composed of quartz, feldspar, pyrite, calcite, dolomite, and clay (Fig. 2). According to the three-

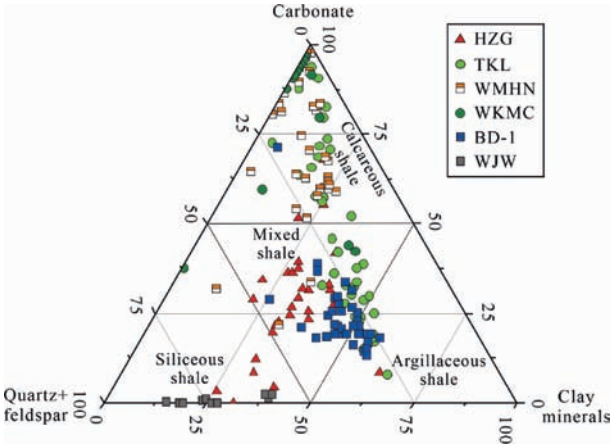


Fig. 2. Ternary diagram of quartz + feldspar, clay minerals and carbonate, showing that the rocks include siliceous, argillaceous and calcareous shales; The borehole and sections include BD-1 (this study), HZG (this study), TKL (this study), WMHN (this study), WK (Yang et al., 2021) and WJW (Yan et al., 2021).

end diagram of the quartz-feldspar, carbonate and clay mineral contents, the LMX Formation in all borehole and sections was composed of siliceous, calcareous, argillaceous and mixed shales (Fig. 2). The LMX Formation in BD-1 was mainly composed of mixed shales in lower part (Figs. 2 and 3A-B) and argillaceous shales in upper part (Figs. 2 and 3B-C). Under the microscope, the mixed shales in BD-1 exhibit a distinctive composition, featuring carbonate-rich laminae interbedded with clay-rich laminae (Fig. 4A–E). Euhedral pyrite was abundant near the boundary between carbonate and clay-rich lamina (Fig. 4A–E) or specifically within the carbonate-rich lamina (Fig. 4F–L). In HZG, the LMX Formation was mainly composed of mixed shales and siliceous shales (Fig. 2). In TKL, the LMX Formation is dominated by calcareous and mixed shales (Fig. 2), and pyrite beds (Fig. 3H–I) can be observed in the lower LMX Formation. In WMHN, the LMX Formation is dominated by calcareous shales (Fig. 2), especially the carbonate beds (Fig. 3D), carbonate concretions (Fig. 3E–G) can be observed.

4.1.2. Calcite

The calcite shows high contents in lower LMX Formation (20%–30%) and low contents in upper LMX Formation (<20%). Based on the crystal size, morphology, and elemental composition, two types of calcites were identified in the shales of BD-1. (1) Calcite cement (Fig. 5A–E): Densely cemented calcite is characterized by a small crystal size (<5 μm) and formed in the vicinity of euhedral calcite or within the pores between quartz and clay minerals (Fig. 5C–E). Furthermore, this type exhibits significantly high Fe contents (>4%, Fig. 5A–B). (2) Euhedral to subhedral crystalline calcite: This type is characterized by large diameters (>10 μm, Fig. 5E–H) and low Fe contents (<1%, Fig. 6A–E). These crystals are widely distributed in carbonate-rich layers (Fig. 4A–B).

4.1.3. Dolomite

The dolomite in LMX Formation of BD-1 shows stable contents (~10%). Based on the crystal size, morphology, and elemental composition, two types of dolomites were identified in the shales of BD-1. (1) Euhedral and subhedral crystalline dolomites: These dolomites typically exhibit rhombohedral crystals, with sizes ranging from 10 to 30 μm (Figs. 5H–I and 6F-I). They commonly have low Fe (<2%) and Mn (<0.2%) contents (Figs. 6F–I and 7F-G). (2) Dolomitic cement: This type generally occurs at the edge of the euhedral dolomite (Figs. 6F–I and 7A-C) and is characterized by high Fe (>2%, Fig. 7G) and Mn contents (>0.2%, Fig. 7F) compared to those of the euhedral and subhedral dolomites.

4.1.4. Pyrite

The pyrite in LMX Formation of BD-1 range from 1% to 4%. Based on the crystal size, morphology, and elemental composition, four types of pyrites (framboidal pyrite, Fig. 5A–B; infilled framboidal pyrite, Fig. 5C–G; pyritic masses, Fig. 5C–G; euhedral pyrite, Figs. 4A–L and 5H-I) were identified in the shales of BD-1. Framboidal pyrite grains exist individually or in clusters. These microcrystals exhibit grains of different sizes, ranging from 1 μm to 15 μm (Fig. 5A–B). Infilled framboids are characterized by a round morphology (Fig. 5C), and several indistinct holes can be observed in these pyrites. The infilled framboids could progressively develop into pyritic masses that were irregular or round in shape, with sizes ranging from 2 μm to 10 μm (Fig. 5D–G). The euhedral pyrite typically features large particles, with sizes ranging from 30 μm to 200 μm (Figs. 4A–L and 5D-G). In addition, these euhedral pyrites commonly occur along the edge of the carbonate-rich layer (Fig. 4A–E) and have high S, Fe, and Co contents (Fig. 7G–I).

4.1.5. Quartz and clay minerals

Quartz has been identified as the important mineral in the LMX shales of BD-1 (15%–30%, Fig. 8), especially the silty quartz has been identified (Figs. 5B and 6A), with these quartz showing large particles (>10 μm) and subangular to angular shapes (Figs. 5B and 6A). Microcrystal quartz is smaller in size(<5 μm) and has a round shape, they generally occur in siliceous shales (e.g. Yang et al., 2018). The clay mineral content varies between 6% and 57% (Fig. 8) with high Al contents (Fig. 7D), and the major clay minerals are characterized by smectite and illite according to previous studies of the LMX Formation (e.g. Ge et al., 2019; Yang et al., 2018).

4.2. Major and trace elements

There is a gradual increase in the Al_2O_3 content from the bottom to the top of the borehole, ranging from 4.2% to 11.1% (average = 7.7%) (Fig. 9). This increasing trend is consistent with the variation in the content of clay minerals. The C_{org}/P ratios vary from 25.7 to 211.9 (average = 103.2) (Fig. 9). The Mo and U concentrations range from 1.4 ppm to 19.0 ppm (average = 6.7 ppm) and from 1.4 ppm to 8.6 ppm (average = 4.7 ppm), respectively (Fig. 9). The Mo_{EF} and U_{EF} ranged from 2.9 to 78.6 (average = 21.4) and from 1.9 to 11.4 (average = 4.3), respectively. The ratios of Ni/Co and V/Cr range from 2.7 to 5.4 (average = 3.4) and from 0.9 to 1.6 (average = 1.2), respectively (Fig. 9).

4.3. Total carbon content (TOC)

The TOC values in BD-1 vary from 0.2% to 1.9% across the entire section and exhibit a decreasing trend from the lower to the upper section (Fig. 9).

4.4. In situ sulfur isotopes of pyrite

Two samples were collected from the shales of BD-1 at 2256.6 m and 2377.5 m to analyze the $\delta^{34}S_{pyr}$ values of euhedral pyrite. The euhedral pyrites with large diameters yield consistently high $\delta^{34}S_{pyr}$ values, ranging from 24.2‰ to 26.5‰ (average = 25.3‰) (Fig. 4D–J).

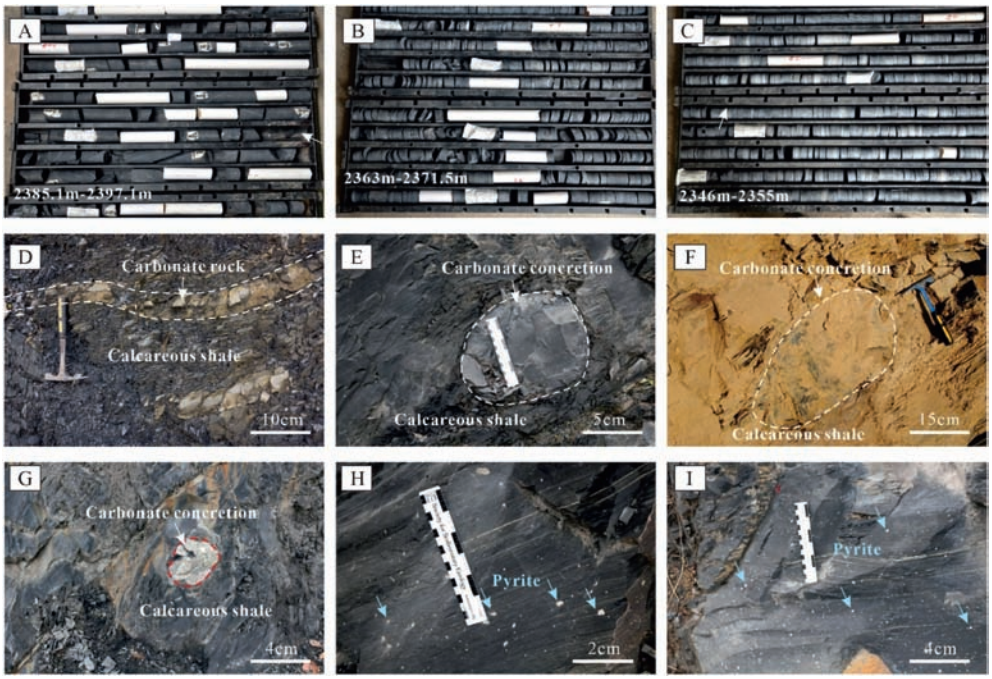


Fig. 3. (A) Core images of BD-1 between 2385.1m and 2397.1 m (LMX Formation). (B) Core images of BD-1 between 2363m and 2371.5 m (LMX Formation). (C) Core images of BD-1 between 2346m and 2355 m (LMX Formation). (D) The carbonate interlayers in WMHN section. (E–G) The carbonate concretion in WMNH section. (H–I) The pyrite layers in TKL section.

5. Discussion

5.1. Evaluation of the redox states

5.1.1. C_{org}/P, redox-sensitive trace elements, and bimetal proxies

Based on the dissolved O_2 levels, the redox states of the water columns were classified as oxic (~> 2 mL/L), dysoxic (~0.2–2 mL/L), suboxic (~0–0.2 mL/L), or anoxic (~0 mL/L) (Tyson and Pearson, 1991). The redox state of seawater during the deposition of shales is typically determined by analyzing multiple redox-sensitive elements (P, U, Mo, V, Ni, and Cr) (Algeo and Tribovillard, 2009; Yan et al., 2012; Zou et al., 2018). Generally, these elements are less susceptible to detrital material and are easily incorporated into sediments that undergo deposition under anoxic water conditions (Algeo and Li, 2020; Tribovillard et al., 2006). Therefore, the contents and ratios of these redox-sensitive elements can serve as reliable indicators of redox states (Algeo and Li, 2020; Jin et al., 2020, 2021; Tribovillard et al., 2006).

In this study, C_{org}/P ratios, Mo–U enrichments, and bimetal proxies were employed to determine the redox states of the water column during the deposition of the LMX shales (Fig. 10). Under oxic-suboxic water conditions, a higher level of phosphorus (P) than of organic carbon (C_{org}) was preserved in the sediments. In this case, the sediments were typically characterized by low C_{org}/P ratios (<~50; Froelich et al., 1979). Under anoxic conditions, the reductive dissolution of Fe-oxyhydroxides led to the release of a large amount of the associated P from the sediments, resulting in high C_{org}/P ratios in the sediments (~>100; Algeo and Ingall, 2007). The enrichment factors for uranium (U) and molybdenum (Mo) are commonly employed as proxies to determine redox water conditions because these elements typically exhibit different properties under highly reducing and oxic conditions in seawater (Algeo and Li, 2020; Algeo and Liu, 2020). Generally, high Mo_{EF} and U_{EF} values indicate an anoxic environment, while low Mo_{EF} and U_{EF} values represent an more oxic environment (Algeo and Li, 2020; Algeo and Liu, 2020). Bimetal proxies, such as V/Cr and Ni/Co, are regarded as reliable proxies for redox states (Hatch and Leventhal, 1992; Jones and Manning, 1994). To summarize, high V/Cr (>4.25) and Ni/Co (>7) ratios are commonly used to indicate anoxic conditions; intermediate V/Cr (2–4.25) and Ni/Co (5–7) ratios indicate dysoxic conditions; and low V/Cr (<2) and Ni/Co (<5) ratios are indicative of oxic conditions.

5.1.2. Anoxic water conditions in the deposition of shales

Previous studies on the depositional environment of the black shales in the LMX Formation revealed that the organic-rich shales in the lower LMX Formation (Rhuddanian) were predominantly deposited in anoxic and sulfidic environments, while the organic-poor argillaceous shales in the upper LMX Formation (Aeronian) were primarily deposited in oxic-suboxic environments (Jin et al., 2020; Xi et al., 2021; Yang et al., 2023).

The shales in lower LMX Formation of BD-1 exhibit relatively high C_{org}/P ratios (>100), high Mo contents (>10 μg/g), high Mo_{EF} (>10) and U_{EF} values (>8) in the lower LMX Formation, indicating anoxic water conditions (Fig. 9). On the other hand, the shales in the upper LMX Formation of BD-1 are characterized by low C_{org}/P ratios (<50 to 100), and low Mo contents (<10 μg/g), low Mo_{EF} (<10) and U_{EF} (<4) values, indicating that the water environment is relatively suboxic. The Mo_{EF} and U_{EF} values in the shales of LMX Formation exhibited a significant decrease trend from the bottom to the top (Figs. 9–10). Also, the shales in the LMX Formation exhibit lowering V/Cr and Ni/Co ratios from lower to upper LMX Formation (Fig. 9), indicating that the bottom waters became more O_2-enriched in the deposition of the LMX Formation. Similarly, Jin et al. (2021) reported contradictory interpretations of redox conditions, probably due to uncertainties in the threshold values of the V/Cr and Ni/Co ratios under different redox conditions. The strong covariances of C_{org}/P with Ni/Co ($R^2 = +0.66$, $p < 0.01$), V/Cr ($R^2 = +0.77$, $p < 0.01$), U_{EF} ($R^2 = +0.79$, $p < 0.01$), and Mo_{EF} ($R^2 = +0.84$, $p < 0.01$) indicate that RSTE, Mo, and U enrichment

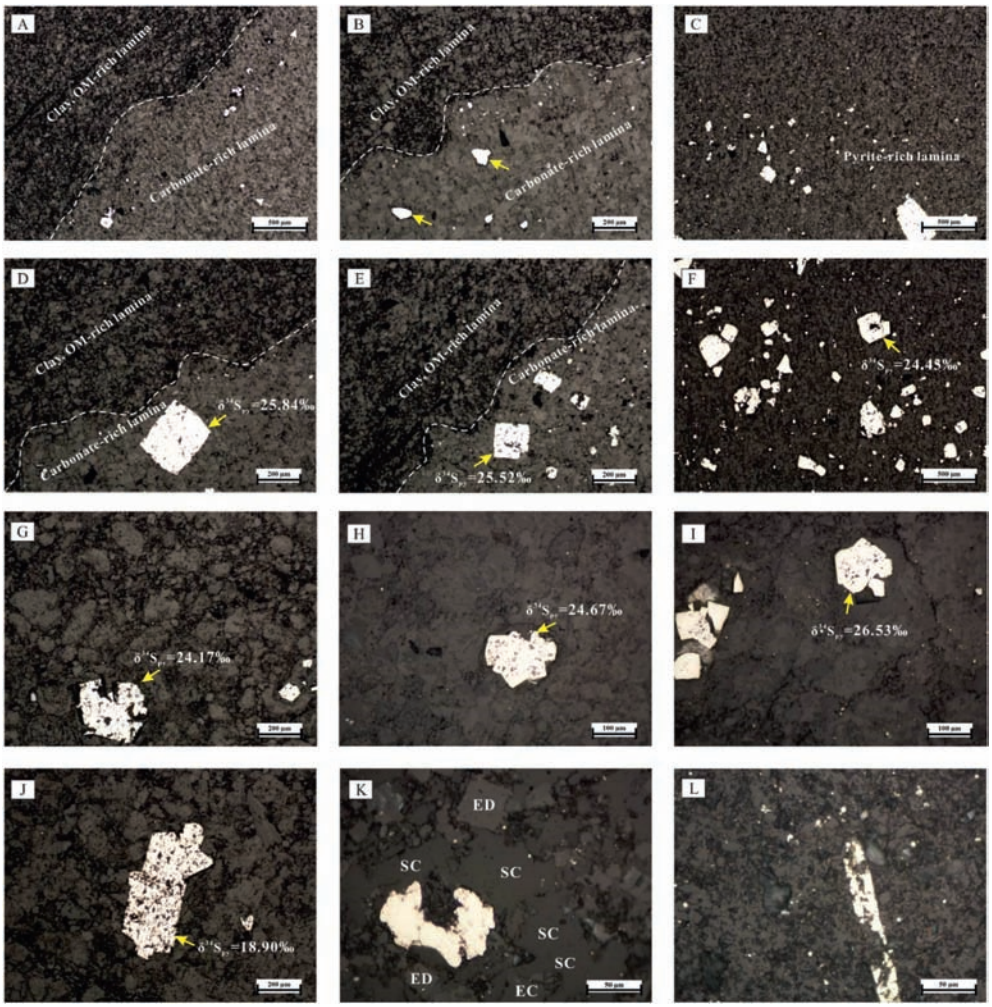


Fig. 4. BD1-3 (2339 m): (A–B) The calcareous shales contain carbonate-rich and clay-rich lamina, and the euhedral pyrites often occur along the edge of carbonate-rich layer. BD1-3 (2339 m): (C) The directional distribution of euhedral pyrite in carbonate-rich lamina. BD1-3 (2339 m): (D–E) The carbonate-rich and clay-rich lamina, with the euhedral pyrites observed in carbonate-rich lamina. BD1-6 (2341.5 m): (F) Abundant euhedral pyrite with high diameters in carbonate-rich lamina. BD1-27 (2364.6 m): (G–L) The euhedral pyrite generally shows large sizes, varying between 30 μm and 200 μm. SC: Subhedral calcite; ED: Euhedral dolomite.

exhibit potential variational trends under redox conditions (Fig. 11A–D). In conclusion, this study revealed that the shales of lower LMX Formation were deposited under anoxic conditions. In contrast, the shales of upper LMX Formation were deposited under oxic-suboxic conditions. This result is consistent with findings from previous studies based on iron speciation, as well as S, Mo, and U isotopic compositions (Jin et al., 2020; Xi et al., 2021; Liu et al., 2022).

5.2. Diagenetic origin of carbon and sulfur isotopic compositions

5.2.1. Diagenesis under anoxic water conditions

Microbial sulfate reduction (MSR) is a ubiquitous process in marine sediments, particularly when the water column above the water-sediment interface is anoxic (Fenchel and Finley, 1995). Under anoxic conditions, sulfate-reducing bacteria utilize SO_4^{2-} as the final electron acceptor for organic matter oxidation (Equation (1)):

$$2CH_2O + SO_4^{2-} \rightarrow H_2S + 2HCO_3^- \quad (1)$$

Methanogenic decomposition of organic matter is the major pathway that occurs during the initial stages of diagenesis, resulting in the production of CH_4 and CO_2 (Equation (2)):

$$2CH_2O \rightarrow CO_2 + CH_4 \quad (2)$$

This process initiates in the deeper region of the sediment column relative to the MSR after the consumption of pore water sulfate (Irwin et al., 1977). The products of methanogenesis exhibit significantly fractionated carbon isotopic compositions, with CH_4 depleted in ^{13}C (~−30‰) in comparison with the generated CO_2 (~48–79‰) (Botz et al., 1996; Whiticar, 1999). Considering a Silurian marine organic matter composition of −30‰, this process would produce CH_4 ($\delta^{13}C$ = ~−70 to −55‰) and CO_2 ($\delta^{13}C$ = ~−5–10‰), as determined by the mass balance approach (Chen et al., 2017; Zan et al., 2022). CH_4 was produced in the methanogenesis zone (MZ), where sulfate was completely consumed. Subsequently, CH_4 diffuses into the transition zone between the sulfate-reducing and methanogenic zones (SMTZ), resulting in the sulfate-driven anaerobic oxidation of methane (SD-AOM; Boetius et al., 2000). In this case, the CH_4 is oxidized by SO_4^{2-} as the final electron receptors to produce CO_2 (Moore et al., 2004) based on the chemical reaction given in Equation (3):

$$CH_4 + SO_4^{2-} + 2H^+ \rightarrow CO_2 + H_2S + 2H_2O \quad (3)$$

In addition, it has also been suggested that anoxic oxidation of methane by Mn- and Fe-oxides could also be observed during early

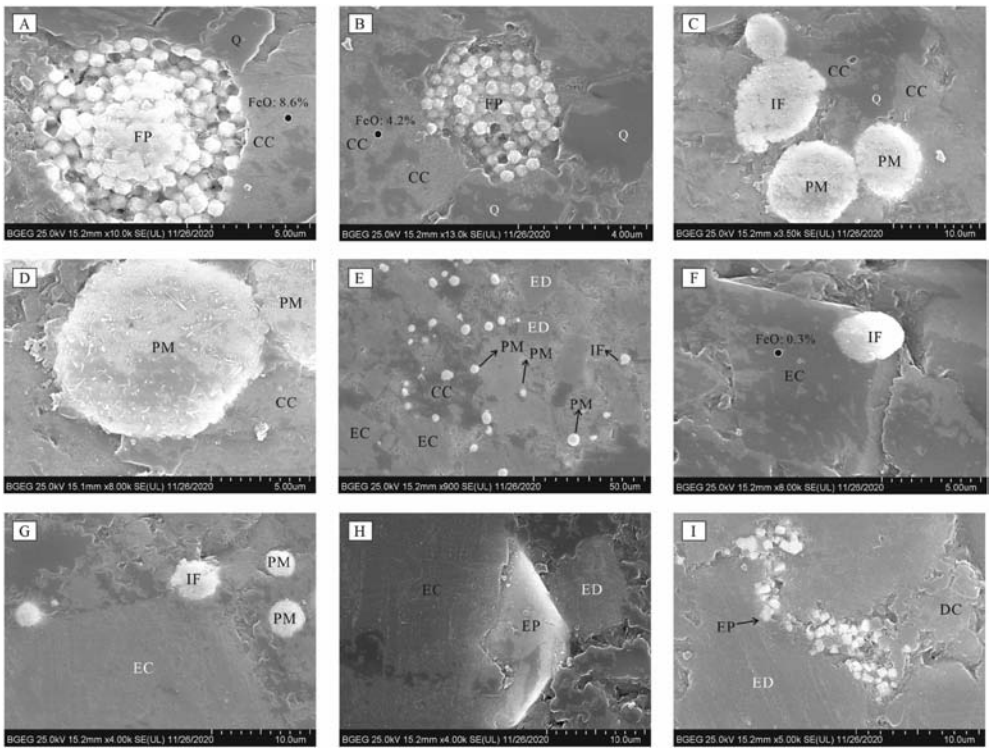


Fig. 5. (A–B) The framboidal pyrite grains display different sizes and the grains varied in diameter from 1 μm to 15 μm. (C–E) Infilled framboids display round morphology, and several indistinct holes can be observed in these pyrites, suggesting a framboidal origin. (F–G) Infilled framboids occur with the euhedral calcite and dolomite. (H–I) Euhedral calcite with high diameters occur with euhedral pyrite. SC: Subhedral calcite; EC: Euhedral calcite; CC: Calcite cement; ED: Euhedral dolomite; FP: Framboidal pyrite; IF: Infilled framboidal. All the figures are from BD1-26 (2361.3 m).

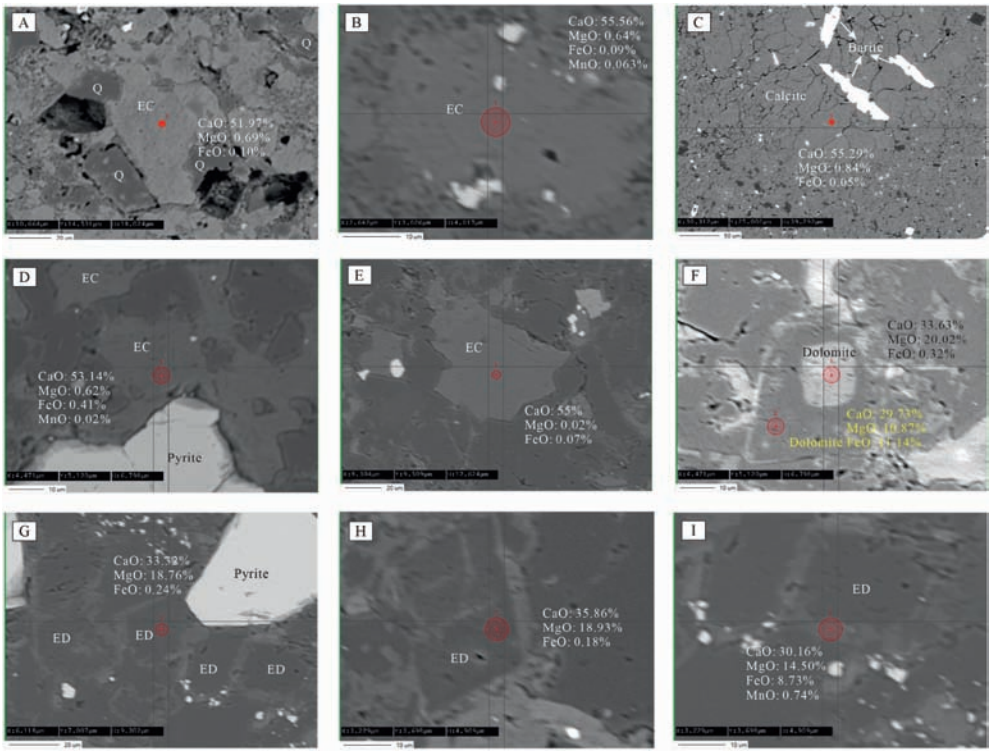


Fig. 6. (A–B) Subhedral calcite with low Fe and Mn contents and silt quartz (>10 μm) are widely distributed in the calcareous shales. (C) Subhedral calcite occurs with barite. (D–E) Subhedral calcite with low Fe and Mn contents. (F–I) Subhedral dolomite with low Fe and Mn contents, and dolomite cement with high Fe and Mn contents. Euhedral calcite with high diameters occurs with euhedral pyrite. Q: Quartz; SC: Subhedral calcite; EC: Euhedral calcite; CC: Calcite cement; ED: Euhedral dolomite; FP: Framboidal pyrite; IF: Infilled framboidal. All the figures are from BD1-16 (2351.6 m).

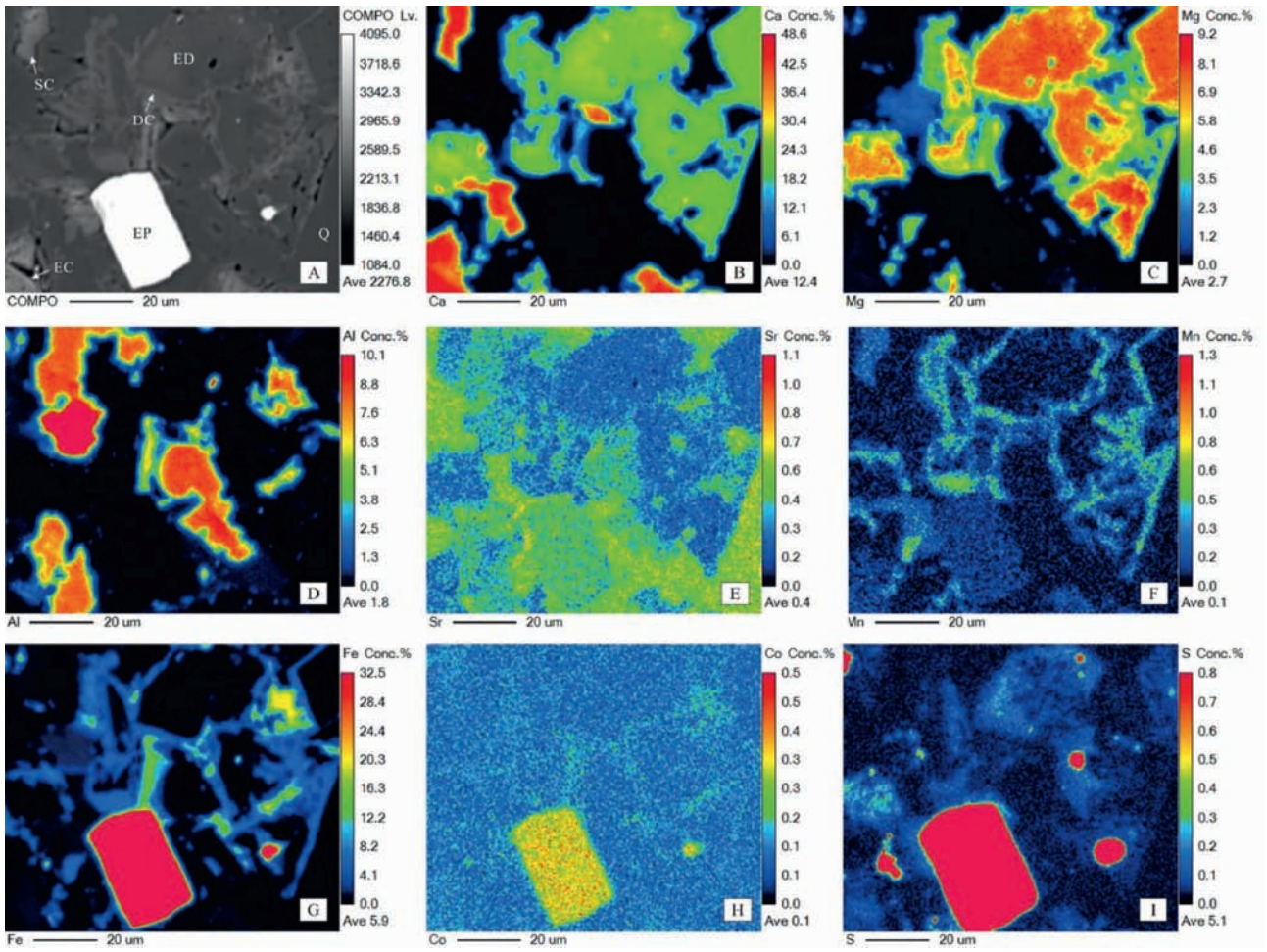


Fig. 7. (A) Back-scattered electron image of the calcite, dolomite, quartz, pyrite and clay minerals. (B) Ca content (C) Mg content, (D) Al content, (E)Sr content, (F) Mn content, (G) Fe content, (H) Co content, (I) S content. EP: Euhedral Pyrite. All the figures are from BD1-26 (2361.3 m).

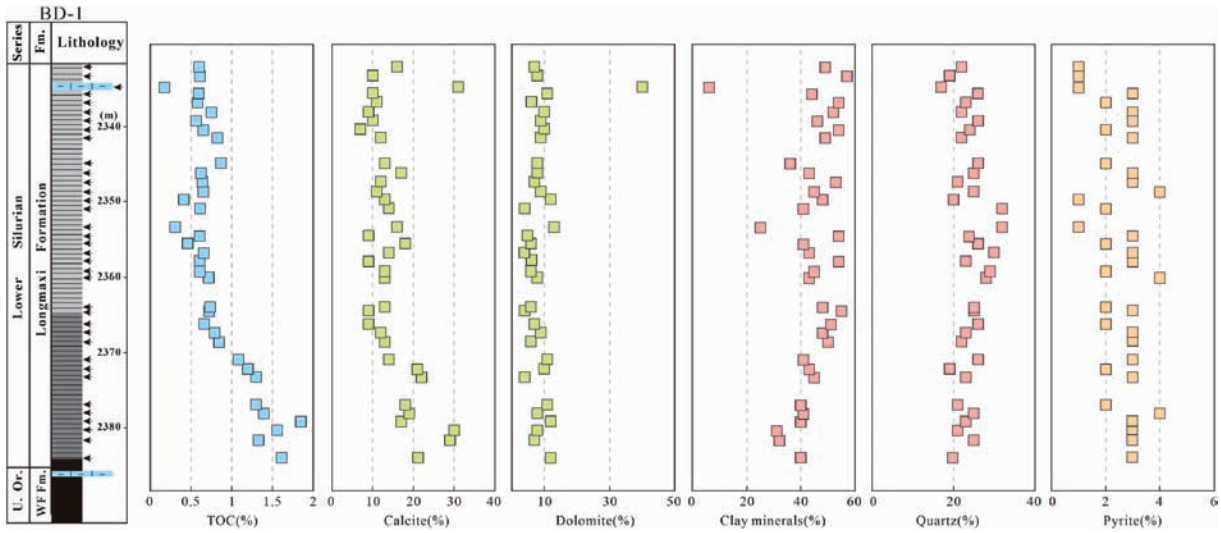


Fig. 8. General trends of TOC, calcite and dolomite, clay minerals, quartz and pyrite contents in the BD-1. U. Or.: Upper Ordovician; Ka.: Katian; WF: Wufeng Formation.

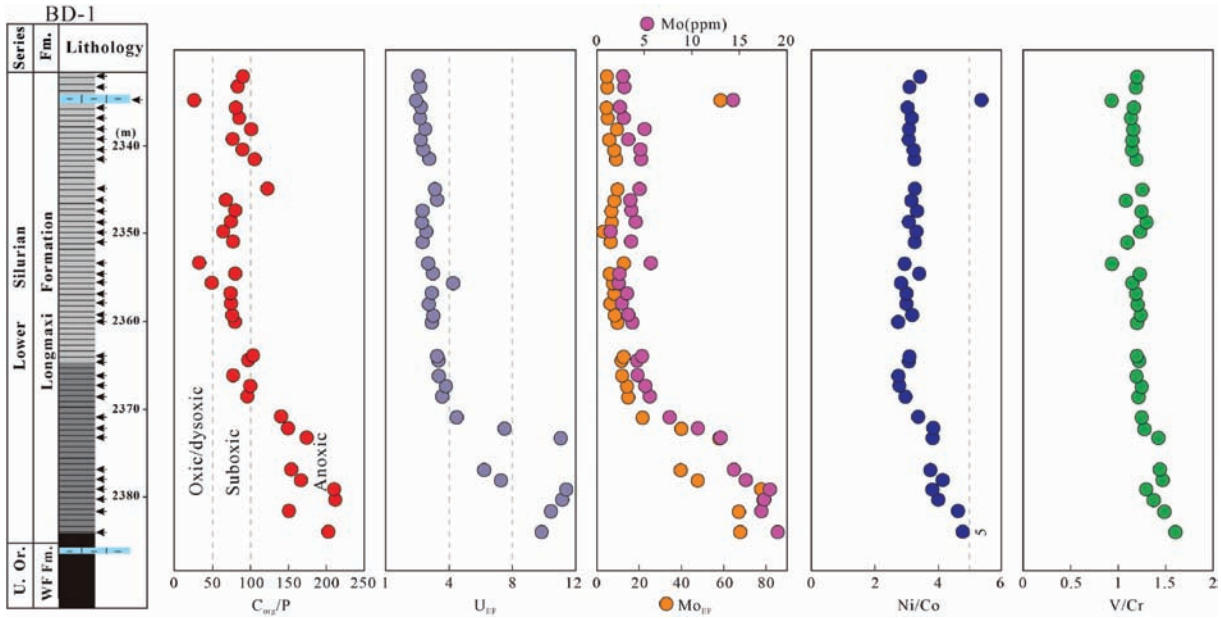


Fig. 9. General trends of U_{EF}, Mo_{EF}, Fe, Mn and Co in the Well-A. U. Or.: Upper Ordovician; Ka.: Katian; WF: Wufeng Formation.

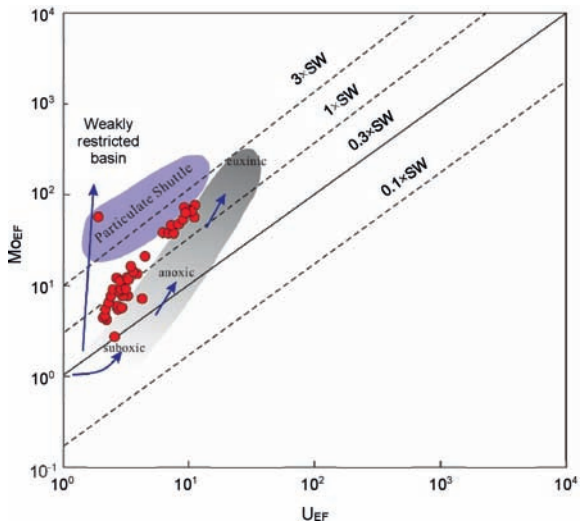


Fig. 10. Cross plots of Mo_{EF} and U_{EF} (Algeo and Li, 2020; Tribovillard et al., 2006).

or late diagenesis (Cai et al., 2021, 2022, 2023; Hu et al., 2018). In this case, high Mn and Fe concentrations would be observed in the calcite or pyrite (Cai et al., 2023) based on the Equation (4):

$$CH_4 + MnO_2 \Big/ Fe_2O_3 + 2H^+ \rightarrow CO_2 + Mn^{2+} \Big/ Fe^{2+} + 2H_2O \quad (4)$$

5.2.2. Early diagenetic origin of carbon isotopic compositions

Numerous studies also highlight the importance of diagenetic carbonate minerals in the organic-rich shales of WF and LMX formations (Chen et al., 2017, 2020; Liu et al., 2022). It has been reported that the marlstones in the Late Ordovician Guanyinqiao Member were characterized by very low $\delta^{13}C_{carb}$ values (<−10‰, Chen et al., 2017, 2020), which is inconsistent with the positive excursion of $\delta^{13}C_{carb}$ (increase from 0‰ to 3‰ in WK section, Liu et al., 2022) in the Hirnantian glaciation. In addition, a large number of carbonate nodules were identified in the shales of the LMX Formation, and these nodules exhibited distinct enrichments in ^{12}C (Chen et al., 2017, 2020). Therefore, the extremely low $\delta^{13}C_{carb}$ values in shales of LMX Formation should be explained by the diagenetic carbon fluxes (MSR and SD-AOM, Chen et al., 2017, 2020; Zan et al., 2022).

Moreover, carbonate-rich and clay-rich layers were identified in the studied shales. The former layer contains a large amount of clay minerals and organic matter, while the latter layer is predominantly composed of calcite and dolomite. Based on the covariational trend of TOC and calcite (Fig. 8) and considering that barite is surrounded by a large amount of carbonate minerals (Fig. 6C), this study suggested that the CO_2 in diagenetic fluid (MSR or SD-AOM) is likely be characterized by low $\delta^{13}C$ values. The ^{12}C-enriched CO_2 in fluid migrated from clay-rich layers to carbonate-rich layers because clay-rich layers generally have low porosity and high pressure.

5.2.3. Early diagenetic origin of sulfur isotopic compositions

Sulfate reduction is one of the primary processes controlling the sulfur cycle (Cai et al., 2022; Machel, 2001). It can be driven by biological activity at temperatures <80 °C (MSR and AOM; Machel, 2001), or it can occur abiotically in hydrothermal fluid or deep burial settings at temperatures >130 °C (thermochemical sulfate reduction, TSR; Orr, 1974; Krouse et al., 1988). The MSR and AOM processes have a preferential microbial turnover of ^{32}S, which results in sulfides with a^{34}S-depleted sulfur isotopic composition (Liang et al., 2024a). In addition, the bulk $\delta^{34}S_{pyr}$ values of TSR-derived pyrites (~18‰, Zhang et al., 2019; Hu et al., 2020) indicate a low degree of fractionation ($\Delta^{34}S_{sulfate\text{-}pyrite} = 10.5‰$).

The euhedral pyrite with large diameters yield consistently high $\delta^{34}S_{pyr}$ values (24.2‰–26.5‰) in the shales of LMX Formation (Fig. 4D–J). Generally, two possibilities could explain these high $\delta^{34}S_{py}$ values, mainly including thermochemical sulfate reduction (Cai et al., 2022), and high sedimentation rates (Liu et al., 2021). First, the diagenetic temperature typically increases as the burial depth increases, which further lead to significant alterations in the mineral composition and the increased $\delta^{34}S_{py}$ values (Cai et al., 2022; Hu et al., 2021; Liang et al., 2024a). The maximum burial

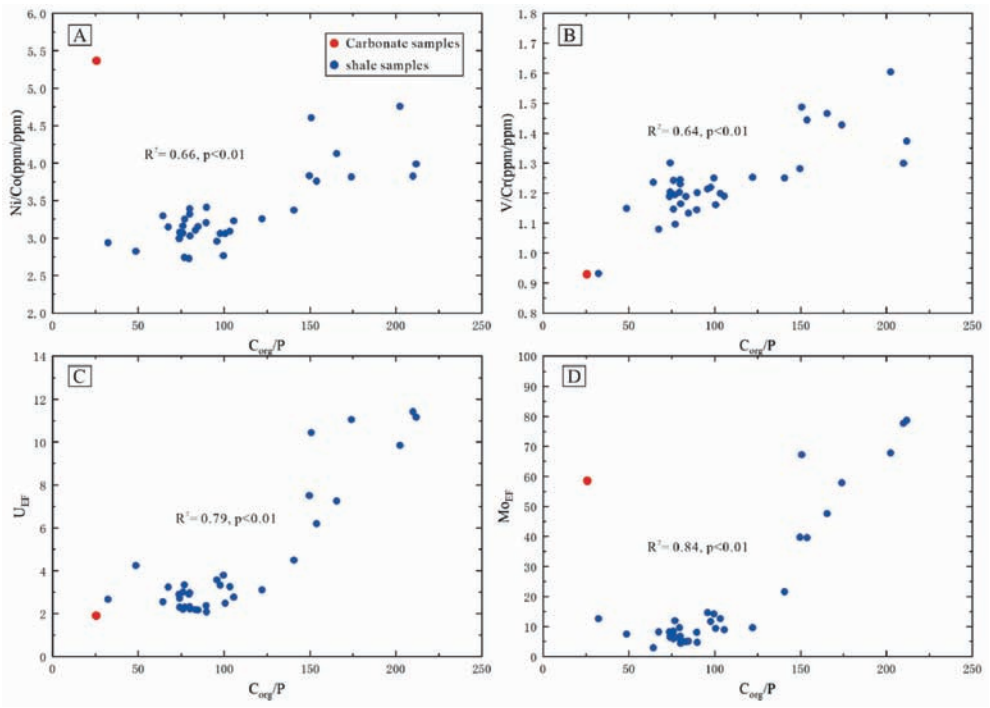


Fig. 11. Cross plots of C_{org}/P and (A) Ni/Co, (B)V/Cr, (C)U_{EF} and (D)Mo_{EF}.

depth of the WF and LMX Formations in the Upper Yangtze area ranges between 2500 m and 4000 m, with organic matter maturity (Ro) ranging from 2% to 4% (Cao et al., 2020; Guo et al., 2020). This indicates that these organic-rich black shales experienced late diagenesis stage with temperatures exceeding 200 °C (Cao et al., 2020; Guo et al., 2020; Lu et al., 2019). However, TSR-derived pyrites are not the main type of pyrite in the shales of LMX Formation which is explained by following reasons: (1) The homogenization temperatures of calcite-vein fluid inclusions in the LMX Formation in Well PY1 range from 128 to 138 °C (Jin et al., 2018; Nie et al., 2020); (2) Clumped isotope-based investigations of the organic-rich dolomite layers in the Guanyinqiao Member underlying the LMX Formation indicate that the formation temperature was below 100 °C (Hu et al., 2022). Both the above calculated temperatures just reach or lower than the minimal temperatures for TSR (>120 °C; Cai et al., 2022). (3) The TSR-derived pyrites are characterized by amorphous and subhedral structure with very small diameters due to heavy compaction and porosity loss during late diagenesis (Hu et al., 2021), which is contrast to the large size (>200 μm) in this study (Fig. 4D–J). Second, high sedimentation rates on $\delta^{34}S_{py}$ were observed at mean rates of ~50 cm/kyr (Pasquier et al., 2017) to >100 cm/kyr (Liu et al., 2021), whereas the LMX shales in studied areas were accumulated at rates of ~39.2 cm/kyr (Zhong et al., 2020).

In this study, the processes of MSR and SD-AOM are likely the main factors controlling the high $\delta^{34}S_{pyr}$ values. Zuo et al. (2021) demonstrated that the $\delta^{34}S_{pyr}$ values of framboidal pyrite in the LMX Formation were approximately −20‰ because the fractionation of sulfur isotopes by sulfate-reducing bacteria corresponded to ~ 16‰–46‰ (Canfield and Raiswell, 1999). If the high $\delta^{34}S_{pyr}$ values are explained by MSR, the deposition environment of pyrite should be very closed within the deep sediments. Alternatively, the high $\delta^{34}S_{pyr}$ values should be explained by SD-AOM under limited sulfate concentrations. The further identification of MSR or AOM-associated pyrites should according to their trace elemental concentrations.

5.3. Formation of calcite-dolomite-pyrite in organic-rich shales

5.3.1. Anoxic water conditions drive the enrichment of organic matter

The amount of organic matter determines the strength of the hydrocarbon generation capacity of shale. It influences the reservoir adsorption capacity and the amount of storage space, which determines the reservoir gas content (Yan et al., 2015; Zou et al., 2010). The enrichment of organic matter is influenced by several factors, including primary productivity and seawater redox conditions (Lu et al., 2019). Among these factors, primary productivity determines the quality of organic matter available for deposition, while redox water conditions play a significant role in organic matter preservation (Jin et al., 2020; Lu et al., 2019). These two factors are considered to be primary determinants that control the deposition of organic-rich shales (Jin et al., 2020; Yan et al., 2015).

The shales in BD-1 exhibit a decrease in the ratios of C_{org}/P, V/(V + Ni), V/Cr, and Ni/Co from the basement to the upper layer (Fig. 9), indicating that the bottom water in the deposition of the LMX Formation underwent a transition from an anoxic to oxic-suboxic environment. The oxidation event during the late LMX period was associated with incongruent weathering (Yang et al., 2023), weak volcanic activity (Li et al., 2021b), and a decrease in sea level (Jin et al., 2020) in the early Silurian.

Based on the covariation of TOC values and redox proxies in BD-1 borehole (Figs. 8–9), this study emphasized the significance of local redox conditions in the regulation of organic matter enrichment. Overall, the combination of sea level rise and congruent weathering driven by melting ice caps resulted in high primary productivity and seawater anoxia, which in turn led to the deposition of organic-rich shales (Yang et al., 2023, 2024).

5.3.2. Degradation of organic matter drove the diagenetic calcite-dolomite-pyrite precipitation in organic-rich shales

An anoxic bottom water environment can promote anaerobic biological activities and the decomposition of organic matter under reducing conditions (e.g., MSR and AOM). These processes can release large amounts of CO_2 and H_2S into pore waters and contribute to the formation of various minerals (Fenchel and Finley, 1995; Yan et al., 2009; Zan et al., 2020). Based on the positive correlation of TOC with calcite (Fig. 8) and pyrite (Fig. 12), we believe there is strong relationship between organic matter and these minerals (calcite and pyrite) in the shales of LMX Formation. Especially, the widely observed low $\delta^{13}C_{carb}$ (<−0.5 ‰ in SH or HG; Chen et al., 2017, 2020) values in shales of LMX suggest that the occurrences of calcite-dolomite should be associated with the addition of ^{12}C derived from decomposition of organic matter (e.g. MSR and SD-AOM). Moreover, the low $\delta^{34}S_{pyr}$ values in both framboidal pyrite (<−20 ‰, Zuo et al., 2021) and bulk shales (−30 ‰ to 0‰, Yan et al., 2009) of LMX Formation were attributed to the decomposition of organic matter due to MSR process.

The formation and evolution of pyrite and carbonate minerals are complex processes, and it is widely accepted that these minerals could form during both the syngenesis and diagenesis (Liang et al., 2024a, 2024b). Generally, framboidal pyrite can form during both syngenesis and diagenesis (Raiswell and Berner, 1985). Syngenetic pyrite forms in euxinic water columns and is characterized by small grain sizes (<5 μm), while diagenetic pyrite contains larger grains (>5 μm) (Berner, 1984; Wilkin and Barnes, 1996). However, Mo–U relationship suggests that the shales in LMX Formation were mainly deposited under anoxia water conditions instead of euxinic conditions (Fig. 10), in which case the diagenetic pyrite should be the dominated type. In this study, the framboidal pyrite are mainly formed due to MSR, as evidenced by their extremely low $\delta^{34}S_{pyr}$ values (~−20 ‰) (Zuo et al., 2021). In addition to the framboidal pyrite, several other types of pyrite (framboidal pyrite, Fig. 5A–B; infilled framboidal pyrite, Fig. 5C–G; pyritic masses, Fig. 5C–G; euhedral pyrite, Figs. 4A–L) have also been observed in the shales of LMX Formation. Recently, it has been suggested the evolution order of pyrite in shales is normal framboids→infilled framboids→overgrown framboids→pyritic masses→euhedral pyrite (Liang et al., 2024a). In their studies, the transformation of normal framboids into infilled framboids/pyritic masses are caused by fluid filling in later stage (e.g. MSR), in which case the infilled framboids/pyritic masses are unrelated to the initial environment (Liang et al., 2024a; Rudmin et al., 2020; Wei et al., 2016). However, euhedral pyrite exhibited higher $\delta^{34}S_{pyr}$ values (24.17‰–26.58‰; Fig. 4D–I) and much greater sizes (>30 μm) than normal/infilled framboidal pyrite (~−20 ‰, Zuo et al., 2021). These high $\delta^{34}S$ values (>20‰) can be driven by both the MSR or SD-AOM processes. The former occurred when the deposition environment of pyrite is very closed within the deep sediments (Gomes and Hurtgen, 2015; Gome et al., 2016). The latter occurred after the MSR, which consumed a large amount of ^{32}S and further resulted in the gradual enrichment of ^{34}S in the sediment pore water (Lin et al., 2016; Chen et al., 2023). Then the ^{34}S-enriched H_2S contributed to the formation of euhedral pyrite with high $\delta^{34}S$ values.

Major (Mn) and trace elements (e.g. Co) in pyrite could provide some insights about the formation of pyrite in early diagenesis (Cai et al., 2021, 2023; Lin et al., 2022; Chen et al., 2023). They found little or no Co was mobilized during early diagenesis, and thus that the Co was mainly unavailable for uptake during formation of MSR-associated pyrite (Chen et al., 2023). In contrast, greater uptake of Co would be observed during the formation of SD-AOM-associated pyrite (Lin et al., 2022; Chen et al., 2023) and greater uptake of Mn in the precipitation of Mn-AOM-associated pyrite (Cai et al., 2021, 2023). Therefore, the MSR-associated pyrite generally shows low Co contents (<100 μg/g); SD-AOM-associated pyrite show high Co contents (can reach 1400 μg/g) (Chen et al., 2023); Mn-AOM-associated pyrite show high Mn contents (can reach 20000 μg/g, Cai et al., 2023). In the shales of LMX Formation, the euhedral pyrites are characterized by extremely high Co contents (>700 μg/g, Table 1; Fig. 7H) and low Mn contents (<2000 μg/g, Fig. 7F), suggesting that these pyrites should be formed due to SD-AOM. Overall, this study suggests that the normal/infilled framboids and pyritic masses were mainly formed due to the MSR, in contrast, the euhedral pyrite were dominantly formed due to the SD-AOM.

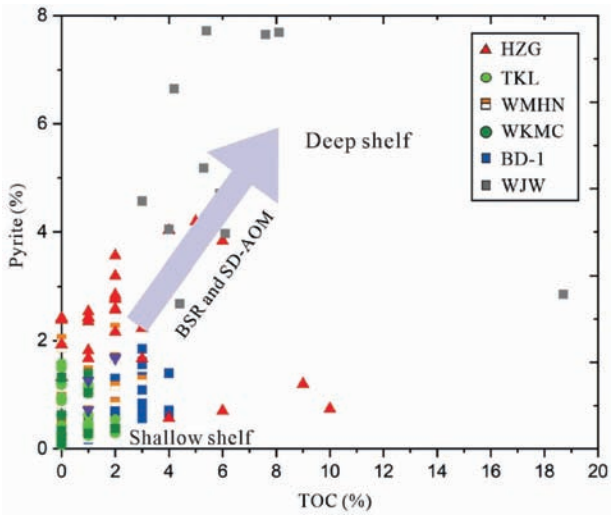


Fig. 12. Cross plots of TOC and pyrite (the datas of WKMC and WJW are from Yang et al., 2021; Yan et al., 2021).

Table 1
The Fe, Co, and S concentrations in Euhedral pyrite; The pyrites are observed in shales of BD1-1, BD1-5, BD1-30, BD1-43.

Sample	Number	Fe(%)	Co(%)	S(%)
BD1-1	PY-1	45.47	0.10	54.00
BD1-1	PY-2	44.58	0.09	55.62
BD1-1	PY-4	45.06	0.06	53.84
BD1-1	PY-5	44.86	0.04	54.37
BD1-5	PY-6	45.68	0.03	54.26
BD1-5	PY-7	45.45	0.04	54.26
BD1-5	PY-8	45.29	0.04	54.20
BD1-5	PY-9	45.30	0.05	54.20
BD1-5	PY-10	45.31	0.05	54.42
BD1-5	PY-11	45.50	0.09	54.35
BD1-5	PY-13	45.43	0.09	54.19
BD1-5	PY-14	45.37	0.08	54.15
BD1-5	PY-15	45.32	0.09	54.16
BD1-5	PY-16	45.34	0.07	54.27
BD1-30	PY-17	45.21	0.10	54.20
BD1-30	PY-18	45.13	0.09	54.35
BD1-30	PY-19	44.01	0.09	53.08
BD1-30	PY-20	43.75	0.09	53.10
BD1-30	PY-21	44.35	0.09	52.74
BD1-30	PY-22	44.07	0.09	53.89
BD1-30	PY-23	43.55	0.07	52.92
BD1-30	PY-24	43.73	0.07	53.40
BD1-43	PY-25	41.95	0.10	50.09
BD1-43	PY-26	45.03	0.07	53.53
BD1-43	PY-27	39.03	0.08	45.86

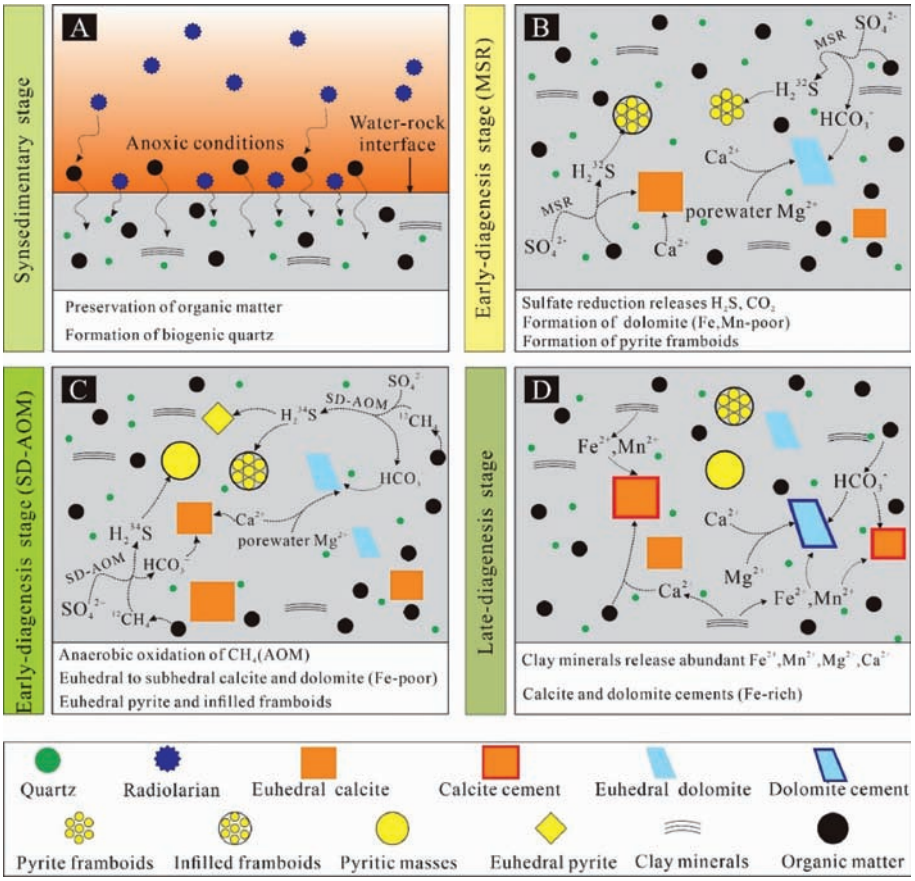


Fig. 13. (A) In synsedimentary stage, the organic matter was well preserved in sediments due to the anoxic water conditions; Meanwhile, the biogenic quartz form due to the abundant radiolarian. (B) A large amount of ^{34}S-depleted framboidal pyrite and calcite formed in pore waters due to the bacterial sulfate reduction (BSR) in the early diagenesis; In addition, BSR increased the Mg^{2+}/SO_4^{2-}, Mg^{2+}/Ca^{2+} ratios, and created a microenvironment favorable to dolomite precipitation with low Fe contents. (C) ^{34}S-riched euhedral pyrite and calcite formed in pore waters due to the anaerobic oxidation of methane (AOM) in the early diagenesis, in which time the Mg^{2+}/SO_4^{2-}, Mg^{2+}/Ca^{2+} ratios increased and abundant euhedral dolomite with low Fe contents precipitated. (D) In the late diagenesis, the decarboxylation of organic matter could release CO_2, which in turn reacts with Ca^{2+} in the pore water to form calcite and dolomite with high Fe contents. These calcite and dolomite mainly occur in the form of cement resulting from the greatly reduced porosity during this period.

Anaerobic oxidation of organic matter (MSR) and methane (SD-AOM) likely contributed to the precipitation of carbonate minerals (calcite and dolomite). This conclusion is supported by the formation of barite (Zan et al., 2022) and carbonate (Chen et al., 2017, 2020) nodules in LMX Formation. In this study, we also observe that the barite is surrounded by calcite and they are likely caused by the MSR and SD-AOM processes (Fig. 6C). Based on the above results, it can be concluded that the biological decomposition of organic matter in the early diagenesis stage provided abudant carbon source and contributed to the formation of carbonate minerals in the shales of the LMX Formation.

5.4. Deposition and diagenesis of the organic-rich shales in Longmaxi Formation

Several studies have indicated a warming climate in the latest Hirnantian and early Silurian (lower LMX Formation) following the Hirnantian glaciation (Yang et al., 2023, 2024). During this period, congruent weathering occurred under the conditions of warming climate and high runoff, as evidenced by low chemical index of alteration (CIA) values (Yang et al., 2023), low $\delta^7Li_{seawater}$ values (Pogge von Strandmann et al., 2017; Yang et al., 2024), and high $^{187}Os/^{188}Os$ ratios (Finlay et al., 2010). The enhanced continental weathering enabled the high primary productivity and expansion of anoxic seawater, leading to the enrichment of organic matter in black shales of LMX Formation (Fig. 13A).

Under such anoxic water conditions and high organic matter contents in sediments, the formation of minerals in organic-rich shales was controlled by the MSR and SD-AOM processes in early diagenesis, and organic-inorganic interactions (e.g. clay transformation, hydrocarbon generation) in late diagenesis.

In the early diagenesis stage, the dissolution of siliceous radiolarians was the primary source of silica (opal A), which is needed for quartz precipitation, either directly or through opal CT, as reported in previous studies (Fig. 13A, Zhao et al., 2017; Yang et al., 2018). The organic matter in the sediments is anaerobically oxidized by the MSR process due to anoxia of waters above the water–rock interface. This process consumed SO_4^{2-} in pore water and produced a large amount of $H_2^{32}S$, which serves as a sulfur source for the formation of framboidal pyrite in pore waters (Fig. 13B). These framboidal pyrites were further transformed into infilled framboids/pyritic masses in the MSR process (Liang et al., 2024a), given their low $\delta^{34}S_{pyr}$ values (Xi et al., 2021; Zuo et al., 2021). Furthermore, a significant amount of CO_2 was released into pore waters during this period, in which time CO_2 could combine with the Ca^{2+} in the pore waters to form calcite.

Later, anaerobic oxidation of organic matter occurs below the SMTZ, where the methanogenic bacteria oxidize organic matter to

generate ^{13}C-depleted CH_4 (Fig. 13C). Oxidation of CH_4 occurs within the SMTZ, in which the ^{13}C-depleted CH_4 diffused upward and reacted with SO_4^{2-} to produce $H_2^{34}S$. The ^{34}S-enriched H_2S is caused by consumption of ^{32}S in the MSR process, then, these $H_2^{34}S$ would combine with Fe^{2+} to form euhedral pyrite with high $\delta^{34}S_{pyr}$ values. Both the MSR and SD-AOM processes gradually decreased the solubility of SO_4^{2-} and Ca^{2+} in the pore waters, thereby increasing both the Mg^{2+}/SO_4^{2-} and Mg^{2+}/Ca^{2+} ratios (Fig. 13B–C). These processes provide a microenvironment conducive to dolomite precipitation. In this case, euhedral dolomites with relatively high diameters but low Fe concentration formed under low temperatures (<110 °C; Hu et al., 2022). This finding is also consistent with previous studies reporting that the dolomite peaks correspond to enhanced sulfate reduction in anoxic environments (Li et al., 2018, 2021; Zuo et al., 2021).

In the late diagenesis stage, the shales of LMX Formation were buried deeper at temperatures higher than 110 °C, in which time the dolomite and calcite cement formed due to low porosity in this stage (Fig. 13D). Interestingly, the carbonate minerals that formed during this stage were characterized by high Fe (>2%) and Mn (>0.2%) concentrations. These high Fe and Mn contents in carbonate minerals should be sourced from the diagenetic fluid and illitization. The LMX shales in South China are overmature (Ro> 2%), with temperatures higher than 100 °C, and multiple stages of fluid activity have been observed (Nie et al., 2020; Wang et al., 2019; Yang et al., 2016). Both the high temperatures and multiple stages of fluids contributed to the formation of Fe- and Mn-rich carbonate minerals. First, the organic acids produced during hydrocarbon generation and migration have a strong reducing capacity. A large amount of organic fluid reacts with the surrounding rocks to release Fe^{2+} and Mn^{2+} ions from clay minerals or volcanic ash into the fluid (Fig. 13D). Second, the conversion of illite to smectite occurs in the late diagenesis stage, as reported by several studies (Wang et al., 2019; Yang et al., 2018). In this process, large amounts of dissolved cations (Na^+, Ca^{2+}, Fe^{2+}, Mn^{2+}, and Mg^{2+}) are released from clay minerals into pore waters. During this process, Fe and Mn substitute mainly for Mg in the dolomite and ankerite crystal lattice, leading to Fe-rich carbonates (e.g., ferrocalcite and ankerite).

5.5. Implications to the climate changes in Early Silurian

The Silurian represents one of the most climatically unstable periods during the Phanerozoic, in which time multiple glaciations and biotic extinction events were observed in global (Grahn and Caputo, 1992; Sproson et al., 2022). In recent, the mechanisms driving the changes in global climate during this period have attracted considerable scholarly attention (Sproson et al., 2022; Yang et al., 2023, 2024). The depositional of the Longmaxi Formation in the South China not only corresponds to the biotic recovery following the Late Ordovician mass extinction, but also coincides with the termination of the Hirnantian glaciation and the subsequent gradual global warming.

Methane is a critical greenhouse gas in the atmosphere, with a warming potential 28 times greater than that of carbon dioxide (Voigt et al., 2017). The anaerobic oxidation of methane (AOM) during early diagenesis in sediments constitutes a key process influencing methane release, making methane seepage events a potential driver of climatic shifts (Bottrell and Newton, 2006). Previous studies have suggested that both volcanic activity and Milankovitch cycles directly or indirectly enhanced paleo-marine productivity, leading to widespread anoxia in bottom waters (Yang et al., 2023, 2024). These anoxic conditions provided a favorable environmental foundation for sulfate-driven AOM during early diagenesis. Consequently, extensive methane release during this period may have contributed to Early Silurian global warming.

6. Conclusions

Two generations of carbonate minerals (calcite and dolomite) are identified in the shales of LMX Formation. (1) Subhedral to euhedral calcite and dolomite with large diameters (>10 μm), as well as low Fe (<1%) and Mn (<0.2%) contents; and (2) calcite and dolomite cement with small diameters (<5 μm), as well as high Fe (>2%) and Mn (>0.2%) contents. In addition, several pyrites, including pyritic masses, euhedral pyrite, framboidal pyrite and infilled framboidal pyrite, are also observed in the shales of LMX Formation.

The formation of calcite-dolomite-pyrite in shales of LMX Formation was likely controlled by both depositional and diagenetic processes. The anoxic water conditions result in the preservation of organic matter in the shales, and provide carbon source for the precipitation of carbonate minerals (calcite and dolomite). In the early diagenesis stage, both the microbial sulfate reduction (MSR) and sulfate-driven anaerobic oxidation of methane (SD-AOM) would generate abundant CO_2, which together with the consumption of SO_4^{2-} further contribute to the formation of carbonate minerals (calcite and dolomite). In addition, the MSR would also release ^{32}S-enriched $H_2^{32}S$ and result in the formation of framboidal pyrite/infilled framboids/pyritic masses with low $\delta^{34}S$ values. However, the SD-AOM would result in the precipitation of euhedral pyrite with high $\delta^{34}S$ values and high Co contents. In the late diagenesis stage, carbonate cements with high Fe and Mn contents formed due to the diagenetic fluids (high HCO_3^- Mg^{2+}, Fe^{2+}, Mn^{2+} concentrations).

The sulfate-driven anaerobic oxidation of methane (AOM) during early diagenesis in sediments constitutes a key process influencing methane release, in which case extensive methane release during this period may have contributed to Early Silurian global warming.

CRediT authorship contribution statement

Yuexiang Hao: Writing – original draft. **Yi Liu:** Writing – review & editing, Methodology, Investigation. **Yibo Zhou:** Writing – review & editing. **Jiexin Li:** Writing – review & editing, Methodology. **Yumeng Jiang:** Writing – review & editing. **Chao Qian:** Writing – review & editing, Methodology. **Xiangrong Yang:** Writing – review & editing.

Acknowledgements

The project was supported by the Natural Science Foundation of China (42402123, 42302175).

References

Algeo, T.J., Tribovillard, N., 2009. Environmental analysis of paleoceanographic systems based on molybdenum–uranium covariation. Chem. Geol. 268, 211–225.

Algeo, T.J., Ingall, E., 2007. Sedimentary C_{org}:P ratios, paleocean ventilation, and Phanerozoic atmospheric pO_2. Palaeogeogr. Palaeoclimatol. Palaeoecol. 256, 130–155.

Algeo, T.J., Li, C., 2020. Redox classification and calibration of redox thresholds in sedimentary systems. Geochem. Cosmochim. Acta 287, 8–26.

Algeo, T.J., Liu, J., 2020. A re-assessment of elemental proxies for paleoredox analysis. Chem. Geol. 540, 119549.

Beauchamp, B., Grasby, S.E., 2012. Permian lysocline shoaling and ocean acidification along NW Pangea led to carbonate eradication and chert expansion. Palaeogeogr. Palaeoclimatol. Palaeoecol. 350–352, 73–90.

Berner, R.A., 1984. Sedimentary pyrite formation: an update. Geochem. Cosmochim. Acta 48, 605–615.

Boetius, A., Ravenschlag, K., Schubert, C.J., Rickert, D., Widdel, F., Gieseke, A., Amann, R., Jorgensen, B.B., Witte, U., Pfannkuche, O., 2000. A marine microbial consortium apparently mediating anaerobic oxidation of methane. Nature 407 (6804), 623–626.

Bonnetti, C., Zhou, L.L., Riegler, T., Brugger, J., Fairclough, M., 2020. Large S isotope and trace element fractionations in pyrite of uranium roll front systems result from internally-driven biogeochemical cycle. Geochem. Cosmochim. Acta 282, 113–132.

Bordiga, M., Beaufort, L., Cobianchi, M., Lupi, C., Mancin, N., Luciani, V., Pelosi, N., Sprovieri, M., 2013. Calcareous plankton and geochemistry from the ODP site 1209B in the NW PacificOcean (Shatsky Rise): new data to interpret calcite dissolution and paleoproductivity changes of the last 450 ka. Palaeogeogr. Palaeoclimatol. Palaeoecol. 371, 93–108.

Bottrell, S.H., Newton, R.J., 2006. Reconstruction of changes in global sulfur cycling from marine sulfate isotopes. Earth Sci. Rev. 75 (1–4), 59–83.

Botz, R., Pokojski, H.D., Schmitt, M., Thomm, M., 1996. Carbon isotope fractionation during bacterial methanogenesis by CO2 reduction. Org. Geochem. 25 (3–4), 255–262.

Cai, C.F., Li, H.X., Li, K.K., Wang, D.W., 2022. Thermochemical sulfate reduction in sedimentary basins and beyond: a review. Chem. Geol. 607, 121018.

Cai, C.F., Li, K.K., Liu, D.W., John, C.M., Wang, D.W., Fu, B., Feng, L.J., Fakhraee, M., Jiang, L., 2021. Anaerobic oxidation of methane by Mn oxides in sulfate-poor environments. Geology 49 (7), 761–766.

Cai, C.F., Liu, D.W., Hu, Y.J., Huang, T.Y., Jiang, Z.W., Xu, C.L., 2023. Interlinked marine cycles of methane, manganese, and sulfate in the post-Marinoan Doushantuo cap dolostone. Geochem. Cosmochim. Acta 346, 245–258.

Cai, C.F., Lyons, T.W., Sun, P., Liu, D.W., Wang, D.W., Tino, C.J., Luo, G.M., Peng, Y.Y., Jiang, L., 2022. Enigmatic super-heavy pyrite formation: novel mechanistic insights from the aftermath of the Sturtian Snowball Earth. Geochem. Cosmochim. Acta 334, 65–82.

Cai, C.F., Worden, R.H., Bottrell, S.H., Wang, L.S., Yang, C.C., 2003. Thermochemical sulphate reduction and the generation of hydrogen sulphide and thiols (mercaptans) in Triassic carbonate reservoirs from the Sichuan Basin, China. Chem. Geol. 202, 39–57.

Canfield, D.E., Raiswell, R., 1999. The evolution of the sulfur cycle. Am. J. Sci. 299, 697–723.

Cao, T.T., Hu, H., Liu, G.X., Deng, M., Cao, Q.G., Yu, Y., 2020. Factors influencing microstructure and porosity in shales of the Wufeng-Longmaxi formations in northwestern Guizhou, China. J. Petrol. Sci. Eng. 191, 107181.

Chalmers, G.R., Bustin, R.M., Power, T.M., 2012. Characterization of gas shale pore-systems by porosimetry, pycnometry, surface area, and field emission scanningelectron microscope/transmission electron microscope image analyses: examples from the Barnett, Woodford, Haynesville, Marcellus, and Doig units. AAPG 96 (6), 1099–1119.

Chen, C., Wang, J.S., Alegeo, T.J., Zhu, J.M., Wang, Z., Ma, X.C., Cen, Y., 2023a. Sulfate-driven anaerobic oxidation of methane inferred from trace-element chemistry and nickel isotopes of pyrite. Geochem. Cosmochim. Acta 349, 81–95.

Chen, C., Wang, J.S., Algeo, T.J., Chen, X.H., Wang, Z., Ma, X.C., Cen, Y., Zhao, J., 2020. New evidence for compaction-driven vertical fluid migration into the Upper Ordovician (Hirnantian) Guanyinqiao bed of south China. Palaeogeogr. Palaeoclimatol. Palaeoecol. 550, 109746.

Chen, C., Wang, J.S., Thomas, J.A., Wang, Z., Tu, S., Wang, G.Z., Yang, J.X., 2017. Negative δ^{13}Ccarb shifts in Upper Ordovician (Hirnantian) Guanyinqiao Bed of South China linked to diagenetic carbon fluxes. Palaeogeogr. Palaeoclimatol. Palaeoecol. 487, 430–446.

Chen, X., Zhang, Y.D., Fan, J.X., Tang, L., Sun, H.Q., 2012. Onset of the Kwangsian Orogeny as evidenced by biofacies and lithofacies. Sci. China Earth Sci. 55, 1592–1600.

Chen, X., Rong, J.Y., Li, Y., Boucot, A.J., 2004. Facies patterns and geography of the Yangtze region, South China, through the Ordovician and Silurian transition. Palaeogeogr. Palaeoclimatol. Palaeoecol. 204, 353–372.

Chen, Y., Zhao, J.H., Hu, Q.H., Liu, K.Y., Wu, W., Luo, C., Zhao, S.H., Zhang, Y.Y., 2023b. Origin of carbonate minerals and impacts on reservoir quality of the Wufeng and Longmaxi Shale, Sichuan Basin. Pet. Sci. 20, 3311–3336.

Fenchel, T., Finlay, B.J., 1995. Ecology and Evolution in Anoxic Worlds. Oxford University Press, New York, p. 276.

Finlay, A.J., Selby, D., Gröcke, D.R., 2010. Tracking the Hirnantian glaciation using Os isotopes. Earth Planet Sci. Lett. 293, 339–348.

Fishman, N.S., Hackley, P.C., Lowers, H.A., Hill, R.J., Egenhoff, S.O., Eberl, D.D., Blum, A.E., 2012. The nature of porosity in organic-rich mudstones of the upperJurassic Kimmeridge clay formation, north sea, offshore United Kingdom. Int. J. Coal Geol. 103, 32–50.

Froelich, P.N., Klinkhammer, G.P., Bender, M.L., Luedtke, N.A., Heath, G.R., Cullen, D., Dauuphin, P., Hammond, D., Hartman, B., Maynard, V., 1979. Early oxidation of organic-matter in pelagic sediments of the eastern equatorial atlantic-suboxic diagenesis. Geochimica et Cosmochimica Acta 43 (7), 1075–1090.

Furmann, A., Mastalerz, M., Bish, D.L., Schimmelmann, A., 2016. Porosity and poresize distribution in mudrocks from the Belle Fourche and Second white Specksformations in Alberta, Canada. AAPG 100 (8), 1265–1288.

Gao, J., He, S., Zhao, J.X., He, Z., Wu, C., Feng, Y., Nguyen, A.D., Zhou, J., Yi, Z., 2019. Sm-Nd isochron dating and geochemical (rare earth elements, ^{87}Sr/^{86}Sr, δ^{18}O, δ^{13}C) characterization of calcite veins in the Jiaoshiba shale gas field, China: Implications for the mechanisms of vein iormation in shale gas systems. Geol. Soc. Am. Bull. 132 (7–8), 1722–1740.

Ge, X.Y., Mou, C.L., Yu, Q., Liu, W., Men, X., He, J., 2019. The geochemistry of the sedimentary rocks from the Huadi no. 1 well in the Wufeng-Longmaxi formations (Upper Ordovician-Lower Silurian), South China, with implications for paleoweathering, provenance, tectonic setting and paleoclimate. Mar. Petrol. Geol. 103, 646–660.

Grahn, Y., Caputo, M.V., 1992. Early Silurian glaciations in Brazil. Palaeogeogr. Palaeoclimatol. Palaeoecol. 99, 9–15.

Gomes, M.L., Hurtgen, M.T., 2015. Sulfur isotope fractionation in modern euxinic systems: implications for paleoenvironmental reconstructions of paired sulfate-sulfide isotope records. Geochem. Cosmochim. Acta 157, 39–55.

Gome, M.L., Hurtgen, M.T., Sageman, B.B., 2016. Biogeochemical sulfur cycling during Cretaceous oceanic anoxic events: a comparison of OAE1a and OAE2. Paleoceanography 31 (2), 233–251.

Gregory, D.D., Large, R.R., Halpin, J.A., Baturina, E.L., Lyons, T.W., Wu, S., Danyushevsky, L., Sack, P.J., Chappaz, A., Maslennikov, V.V., Bull, S.W., 2015. Trace element content of sedimentary pyrite in Black shales. Econ. Geol. 110, 1389–1410.

Guo, X.S., Li, Y.P., Borjigen, T., Wang, Q., Yuan, T., Shen, B.J., Ma, Z.L., Wei, F.B., 2020. Hydrocarbon generation and storage mechanisms of deep water shelf shales of Ordovician Wufeng Formation–Silurian Longmaxi Formation in Sichuan Basin, China. Petrol. Explor. Dev. 47 (1), 204–213.

Hatch, J.R., Leventhal, J.S., 1992. Relationship between inferred redox potential of the depositional environment and geochemistry of the Upper Pennsylvanian (Missourian) Stark Shale Member of the Dennis Limestone, Wabaunsee County, Kansas, U.S.A. Chem. Geol. 99, 65–82.

Hinrichs, K.U., Hayes, J.M., Sylva, S.P., Brewer, P.G., DeLong, E.F., 1999. Methane-consuming archaebacteria in marine sediments. Nature 398 (6730), 802–805.

Hu, Q.H., Ewing, R.P., Rowe, H.D., 2015. Low nanopore connectivity limits gas production in Barnett formation. J. Geophys. Res. Solid Earth 120 (12), 8073–8087.

Hu, W.X., Kang, X., Cao, J., Wang, X.L., Fu, B., Wu, H.G., 2018. Thermochemical oxidation of methane induced by high-valence metal oxides in a sedimentary basin. Nat. Commun. 9, 5131.

Hu, X.L., Müller, I.A., Zhao, A.K., Ziegler, M., Chen, Q., Han, L., Shi, Z.Q., 2022. Clumped isotope thermometry reveals diagenetic origin of the dolomite layer within late Ordovician black shale of the Guanyinqiao Bed (SW China). Chem. Geol. 588, 120641.

Hu, Y.J., Cai, C.F., Liu, D.W., Peng, Y.Y., Wei, T.Y., Jiang, Z.W., Ma, R.T., Jiang, L., 2021. Distinguishing microbial from thermochemical sulfate reduction from the upper Ediacaran in South China. Chem. Geol. 583, 120482.

Hu, Y.J., Cai, C.F., Pederson, C.L., Liu, D.W., Jiang, L., He, X.Y., Shi, S.Y., Immenhauser, A., 2020. Dolomitization history and porosity evolution of a giant, deeply buried Ediacaran gas field (Sichuan Basin, China). Precambr. Res. 338, 105595.

Irwin, H., Curtis, C., Coleman, M., 1977. Isotopic evidence for source of diagenetic carbonates formed during burial of organic-rich sediments. Nature 269, 209–213.

Jin, C., Li, C., Algeo, T.J., O'Connell, B., Cheng, M., Shi, W., Shen, J., Planavsky, N.J., 2018. Highly heterogeneous “poikiloredox” conditions in the early Ediacaran Yangtze Sea. Precambr. Res. 311, 157–166.

Jin, C.S., Liao, Z.W., Tang, Y.J., 2020. Sea-level changes control organic matter accumulation in the Longmaxi shales of southeastern Chongqing, China. Mar. Petrol. Geol. 119, 104478.

Jin, C.S., Liao, Z.W., Tang, Y.J., 2021. High-frequency redox variation across the Ordovician–Silurian transition, South China. Palaeogeogr. Palaeoclimatol. Palaeoecol. 566 (15), 11028.

Jones, B., Manning, D.A.C., 1994. Comparison of geochemical indices used for the interpretation of palaeoredox conditions in ancient mudstones. Chem. Geol. 111, 111–129.

Krouse, H.R., Viau, C.A., Eliuk, L.S., Ueda, A., Halas, S., 1988. Chemical and isotopic evidence of thermochemical sulfate reduction by light hydrocarbon gases in deep carbonate reservoirs. Nature 333, 415–419.

Li, K., Xi, K.L., Cao, Y.C., Shan, X., Lin, M.R., 2024. Diagenetic alterations induced by lamina-scale mass transfer and theimpacts on shale oil reservoir formation in carbonate-rich shale of the Permian Lucaogou Formation, Jimusar Sag. Mar. Petrol. Geol. 162, 106709.

Li, M.T., Song, H.J., Algeo, T.J., Wignall, P.B., Dai, X., Woods, A.D., 2018. A dolomitization event at the oceanic chemocline during the Permian-Triassic transition. Geology 46, 1043–1046.

Li, M.T., Wignall, P.B., Dai, X., Hu, M.Y., Song, H.J., 2021a. Phanerozoic variation in dolomite abundance linked to oceanic anoxia. Geology 49 (6), 698–702.

Li, Q., You, X., Jiang, Z., Wu, S., Zhang, R., 2020. The origins of carbonate minerals of asource-controlled lacustrine carbonate succession in the Shulu sag, Bohai Bay basin:implications for porosity development and paleoenvironment. Mar. Petrol. Geol. 122, 104673.

Li, Y.F., Zhang, T.W., Shen, B.J., Li, Z.M., Shao, D.Y., Lash, G.G., 2021b. Carbon and sulfur isotope variations through the Upper Ordovician and Lower Silurian of South China linked to volcanism. Palaeogeogr. Palaeoclimatol. Palaeoecol. 567, 110285.

Liang, C., Ji, S.C., Cao, Y.C., Liu, K.Y., Wu, J., Hao, F., 2024a. Characteristics, origins, and significance of pyrites indeep-water shales. Sci. China Earth Sci. 67 (2), 313–342.

Liang, C., Wang, J.R., Cao, Y.C., Xiong, Z.H., Liu, K.Y., Hao, F., Han, W.L., 2024b. Authigenic calcite in shales: implications for tracing burial processes and diagenetic fluid evolution in sedimentary basins. Earth Sci. Rev. 258, 104935.

Lin, Z., Sun, X., Chen, K., Strauss, H., Klemd, R., Smrzka, D., Chen, T., Lu, Y., Peckmann, J., 2022. Effects of sulfate reduction processes on the trace element geochemistry of sedimentary pyrite in modern seep environments. Geochem. Cosmochim. Acta 333, 75–94.
Lin, Z., Sun, X., Peckmann, J., Lu, Y., Xu, L., Strauss, H., Zhou, H., Gong, J., Lu, H., Teichert, B.M.A., 2016. How sulfate-driven anaerobic oxidation of methane affects the sulfur isotopic composition of pyrite: a SIMS study from the South China Sea. Chem. Geol. 440, 26–41.
Lisitzin, A.P., 1972. Sedimentation in the world ocean. Soc. Econ. Paleontol. Mineral. Spec. Publ. 17, 218.
Liu, J., Antler, G., Pellerin, A., Izon, G., Dohrmann, I., Findlay, A.J., Røy, H., Ono, S., Turchyn, A.V., Kasten, S., Jørgensen, B.B., 2021. Isotopically "heavy" pyrite in marine sediments due to high sedimentation rates and non-steady-state deposition. Geology 49 (7), 816–821.
Liu, M., Chen, D.Z., Jiang, L., 2022. Oceanic anoxia and extinction in the latest Ordovician. Earth Planet Sci. Lett. 588, 117553.
Liu, X., Meng, S.W., Liang, Z.Z., Tang, C.A., Tao, J.P., Tang, J.Z., 2023. Microscale crack propagation in shale samples using focused ion beam scanning electron microscopy and three-dimensional numerical modeling. Pet. Sci. 20, 1488–1512.
Liu, Y., Hu, W., Cao, J., Wang, X., Zhu, F., Tang, Q., Gao, W., 2019. Fluid–rock interaction and its effects on the Upper Triassic tight sandstones in the Sichuan Basin, China: insights from petrographic and geochemical study of carbonate cements. Sediment. Geol. 383, 121–135.
Liu, Z.H., Algeo, T.J., Guo, X., Fan, J.X., Du, X.B., Lu, Y.C., 2017. Paleo-environmental cyclicity in the Early Silurian Yangtze Sea (South China): tectonic or glacio-eustatic control? Palaeogeogr. Palaeoclimatol. Palaeoecol. 466, 59–76.
Lu, Y.B., Jiang, S., Lu, Y.C., Xu, S., Shu, Y., Wang, Y.X., 2019. Productivity or preservation? The factors controlling the organic matter accumulation in the late Katian through Hirnantian Wufeng organic-rich shale, South China. Mar. Petrol. Geol. 109, 22–35.
Machel, H.G., 2001. Bacterial and thermochemical sulphate reduction in diagenetic settings – old and new insights. Sediment. Geol. 140, 143–175.
Moore, T.S., Murray, R., Kurtz, A., Schrag, D., 2004. Anaerobic methane oxidation and the formation of dolomite. Earth Planet Sci. Lett. 229 (1), 141–154.
Mou, C., Ge, X., Xu, X.S., Zhou, K.K., Wei, L., Wang, X.P., 2014. Lithofacies palaeogeography of the Late Ordovician and its petroleum geological significance in Middle – upper Yangtze Region. J. Palaeogeogr. 16 (4), 428–440.
Nie, H.K., He, Z.L., Wang, R.Y., Zhang, G.R., Chen, Q., Li, D.H., Lu, Z.Y., Sun, C.X., 2020. Temperature and origin of fluid inclusions in shale veins of Wufeng–Longmaxi Formations, Sichuan Basin, south China: implications for shale gas preservation and enrichment. J. Petrol. Sci. Eng. 193, 107329.
Orr, W.L., 1974. Changes in sulfur content and isotopic ratios of sulfur during petroleum maturation -study of big Horn Basin Paleozoic oils. AAPG Bull. 58, 2295–2318.
Pasquier, V., Sansjofre, P., Rabineau, M., Revillon, S., Houghton, J., Fike, D.A., 2017. Pyrite sulfur isotopes reveal glacial-interglacial environmental changes. PNAS 114 (23), 5941–5945.
Pogge von Strandmann, P.A.E., Desrochers, A., Murphy, M.J., Finlay, A.J., Selby, D., Lenton, T.M., 2017. Global climate stabilisation by chemical weathering during the Hirnantian glaciation. Geochem. Pers. Lett. 3, 230–237.
Raiswell, R., Berner, R.A., 1985. Pyrite formation in euxinic and semi-euxinic sediments. Am. J. Sci. 285, 710–724.
Roberts, J.A., Bennett, P.C., Gonzalez, L.A., Macpherson, G., Milliken, K.L., 2004. Microbial precipitation of dolomite in methanogenic groundwater. Geology 32 (4), 277–280.
Rudmin, M., Banerjee, S., Abdullayev, E., Ruban, A., Filimonenko, E., Lyapina, E., Kashapov, R., Mazurov, A., 2020. Ooidal ironstones in the Meso-Cenozoic sequences in western Siberia: assessment of formation processes and relationship with regional and global earth processes. J. Palaeogeogr. 9, 1–21.
Sanchez-Roman, M., McKenzie, J.A., Wagener, A., Rivadeneyra, M.A., Vasconcelos, C., 2009. Presence of sulfate does not inhibit low-temperature dolomite precipitation. Earth Planet Sci. Lett. 285 (1), 131–139.
Slack, J.F., McAleer, R.J., Shanks, W.C., Dumoulin, J.J., 2021. Diagenetic barite-pyrite-wurtzite Formation and redox signatures in Triassic Mudstone, Brooks Range, Northern Alaska. Chem. Geol. 585, 120568.
Sproson, A.D., Pogge von Strandmann, P.A.E., Selby, D., Jarochowska, E., Fryda, J., Hladil, J., Loydell, D.K., Slavik, L., Calner, M., Maier, G., Munnecke, A., Lenton, T. M., 2022. Osmium and lithium isotope evidence for weathering feedbacks linked to orbitally paced organic carbon burial and Silurian glaciations. Earth Planet Sci. Lett. 577, 117260.
Sun, F.L., Hu, W.X., Hu, H.G., Fu, B., Wang, X.L., Tang, Y., Cao, J., Yang, S.C., Hu, Z.Y., 2021. Two-stage mineral dissolution and precipitation related to organic matter egradation: insights from in situ C–O isotopes of zoned carbonate cements. Mar. Petrol. Geol. 124, 104812.
Taylor, S.R., McLennan, S.M., 1985. The Continental Crust: Its Composition and Evolution. Blackwell, Oxford, p. 312.
Tribovillard, N., Algeo, T.J., Lyons, T., Riboulleau, A., 2006. Trace metals as paleoredoxand paleoproductivity proxies: an update. Chem. Geol. 232, 12–32.
Tyson, R.V., Pearson, T.H., 1991. Modern and ancient continental shelf anoxia: an overview. In: Tyson, R.V., Pearson, T.H. (Eds.), Modern and Ancient Continental Shelf Anoxia, vol. 58. Geological Society Special Publication, pp. 1–24.
Voigt, C., Lamprecht, R.E., Marushchak, M.E., Lind, S.E., Novakovskiy, A., Aurela, M., Martikainen, P.J., Biasi, C., 2017. Warming of subarctic tundra increases emissions of all three important greenhouse gases—Carbon dioxide, methane, and nitrous oxide. Glob. Change Biol. 23, 3121–3138.
Wang, Y., Qiu, N.S., Borjigin, T., Shen, B.J., Xie, X.M., Ma, Z.L., Lu, C.J., Yang, Y.F., Yang, L., Cheng, L.J., Fang, G.J., Cui, Y., 2019. Integrated assessment of thermal maturity of the upper ordovician–lower silurian wufeng–longmaxi shale in Sichuan Basin, China. Mar. Petrol. Geol. 100, 447–465.
Wei, H.Y., Wei, X.M., Qiu, Z., Song, H.Y., Shi, G., 2016. Redox conditions across the G–L boundary in South China: evidence from pyrite morphology and sulfur isotopic compositions. Chem. Geol. 440, 1–14.
Whiticar, M.J., 1999. Carbon and hydrogen isotope systematics of bacterial formation and oxidation of methane. Chem. Geol. 161 (1), 291–314.
Wilkin, R.T., Barnes, H.L., 1996. Pyrite formation by reactions of iron monosulfides with dissolved inorganic and organic sulfur species. Geochem. Cosmochim. Acta 60, 4167–4179.
Wu, A.B., Zhang, J.K., Wang, J.L., Luo, J.G., Luo, Q., Jiang, Z.X., 2020. Genesis,diagenetic model and geological significance of calcite veins in organic-rich shale: a case study of the Longmaxi Formation, southern Sichuan basin, China. Geol. Rev. 66 (1), 88–100.
Xi, Z.D., Tang, S.H., Lash, G.G., Zhang, B., Lin, D.L., 2021. Geochemical characteristics of organic carbon and pyrite sulfur in Ordovician-Silurian transition shales in the Yangtze Platform, South China: implications for the depositional environment. Palaeogeogr. Palaeoclimatol. Palaeoecol. 563, 110173.
Xie, D.L., Yao, S.P., Cao, J., Hu, W.X., Qin, Y., 2020. Origin of calcite cements and their impact on reservoir heterogeneity in the Triassic Yanchang Formation, Ordos Basin, China: a combined petrological and geochemical study. Mar. Petrol. Geol. 117, 104376.
Yan, D.T., Chen, D.Z., Wang, Q.C., Wang, J.G., 2012. Predominance of stratified anoxic Yangtze Sea interrupted by short-term oxygenation during the Ordo-Silurian transition. Chem. Geol. 291, 69–78.
Yan, D.T., Li, S.J., Fu, H.J., Jasper, D.M., Zhou, S.D., Yang, X.R., Zhang, B., Mangi, H.N., 2021. Mineralogy and geochemistry of Lower Silurian black shales from the Yangtze platform, South China. Int. J. Coal Geol. 237, 103706.
Yan, D.T., Chen, D.Z., Wang, Q.C., Wang, J.G., Wang, Z.Z., 2009. Carbon and sulfur isotopic anomalies across the Ordovician-Silurian boundary on the Yangtze Platform, South China. Palaeogeogr. Palaeoclimatol. Palaeoecol. 274, 32–39.
Yan, D.T., Wang, H., Fu, Q.L., Chen, Z.H., He, J., Gao, Z., 2015. Geochemical characteristics in the Longmaxi Formation (Early Silurian) of South China: implications for organic matter accumulation. Mar. Petrol. Geol. 65, 290–301.
Yang, R., He, S., Wang, X., Hu, Q.H., Hu, D.F., Yi, J.Z., 2016. Paleo-ocean redox environments of the upper ordovician Wufeng and the first member in lower silurian Longmaxi formations in the Jiaoshiba area, Sichuan Basin. Can. J. Earth Sci. 53, 426–440.
Yang, X.R., Yan, D.T., Chen, D.Z., Liu, M., She, X.H., Zhang, B., Zhang, L.W., Zhang, J.F., 2021. Spatiotemporal variations of sedimentary carbon and nitrogen isotopic compositions in the Yangtze Shelf Sea across the Ordovician-Silurian boundary. Palaeogeogr. Palaeoclimatol. Palaeoecol. 567, 110257.
Yang, X.R., Yan, D.T., Wei, X.S., Zhang, L.W., Zhang, B., Xu, H.W., Gong, Y., He, J., 2018. Different formation mechanism of quartz in siliceous and argillaceous shales: a case study of Lungmachi Formation in South China. Mar. Petrol. Geol. 94, 80–94.
Yang, X.R., Yan, D.T., Wilson, D.J., Pogge von Strandmann, P.A.E., Liu, X.Y., Liu, C.Y., Liu, M., Zhang, L.W., Zhang, B., Chen, D.Z., 2024. Lithium isotope and mercury evidence for enhanced continental weathering and intense volcanism during the Ordovician-Silurian transition. Geochem. Cosmochim. Acta 391, 49–68.
Yang, X.R., Yan, D.T., Zhang, B., Zhang, L.W., 2023. Anomalous weathering trends during the early Silurian warming: implications for the biotic crisis and recovery. Palaeogeogr. Palaeoclimatol. Palaeoecol. 632, 111859.
Yang, X.R., Yan, D.T., Zhang, B., Zhang, L.W., Wei, X.S., Li, T., He, J., Shangguan, Y.F., Zhang, M.X., She, X.H., 2020. The depositional mechanism of organic-rich siliceous shales in Upper Yangtze area: response to the Kwangsian Orogeny in South China. J. Petrol. Sci. Eng., 107310
Zan, B.W., Mou, C.L., Lash, G.G., Yan, J.X., Hou, Q., 2022. Diagenetic barite-calcite-pyrite nodules in the Silurian Longmaxi Formation of the Yangtze Block, South China: a plausible record of sulfate-methane transition zone movements in ancient marine sediments. Chem. Geol. 595, 120789.
Zan, B.W., Yan, J.X., Liu, S.G., Mou, C.L., Ran, B., 2020. Llandovery (lower Silurian) nodular barite from the northern margin of Yangtze Block, South China, and its paleoceanographic implications. Palaeogeogr. Palaeoclimatol. Palaeoecol. 537, 109415.
Zhang, G.W., Guo, A.L., Wang, Y.J., Li, S.Z., Dong, Y.P., Liu, S.F., He, D.F., Cheng, S.Y., Lu, R.K., Yao, A.P., 2013. Tectonics of South China continent and its implications. China Earth Sci. 56, 1804–1828.
Zhang, P., Liu, G., Cai, C., Li, M., Chen, R., Gao, P., Xu, C., Wan, W., Zhang, Y., Jiang, M., 2019. Alteration of solid bitumen by hydrothermal heating and thermochemical sulfate reduction in the Ediacaran and Cambrian dolomite reservoirs in the Central Sichuan Basin, SW China. Precambr. Res. 321, 277–302.
Zhao, J.H., Jin, Z.K., Jin, Z.J., Geng, Y., 2017. Origin of authigenic quartz in organic-rich shales of the Wufeng and Longmaxi Formations in the Sichuan Basin, South China: implications for pore evolution. J. Nat. Gas Sci. Eng. 38, 21–38.

Zhong, Y.Y., Wu, H.C., Fan, J.X., Fang, Q., Shi, M.N., Zhang, S.H., Yang, T.S., Li, H.Y., Cao, L. W., 2020. Late Ordovician obliquity-forced glacio-eustasy recorded in the YangtzeBlock, South China. Palaeogeogr. Palaeoclimatol. Palaeoecol. 540, 109520.

Zou, C.N., Dong, D.Z., Wang, S.J., Li, J.Z., Li, X.J., Wang, Y.M., Li, D.H., Cheng, K.M., 2010. Geological characteristics and resource potential of shale gas in China. Petrol. Explor. Dev. 37, 641–653.

Zou, C.N., Qiu, Z., Wei, H.Y., Dong, D.Z., Liu, B., 2018. Euxinia caused the late Ordovician extinction: evidence from pyrite morphology and pyritic sulfur isotopic composition in the Yangtze area, South China. Palaeogeogr. Palaeoclimatol. Palaeoecol. 511, 1–11.

Zuo, Q.W., Xu, Y.R., Yu, B.S., Zhang, C., Zhang, Y.F., Hou, C.H., Zhang, L.H., Sun, M.D., 2021. Nano SIMS sulfur isotope studies of pyrite from the early Paleozoic marine shale: implications for the sedimentary environment. Mar. Petrol. Geol. 124, 104802.